Journal of Catalysis 434 (2024) 115518

Contents lists available at ScienceDirect

Journal of Catalysis

journal homepage: www.elsevier.com/locate/jcat

Research article

Influence of acid strength on olefin selectivity of chabazite (CHA) framework zeolite/zeotype during tandem CO_2 hydrogenation

Fatima Mahnaz, Jasan Robey Mangalindan, Jenna Vito, Ryan Helmer, Manish Shetty [*]

Artie McFerrin Department of Chemical Engineering, Texas A&M University College Station, TX 77843, United States

ARTICLE INFO

Keywords:
C–C coupling
Zeolite
Ion exchange
MTO
Hydrocarbon
Methanol
Tandem
Hydrogenation

ABSTRACT

The role of Brønsted acid sites (BAS) strength of chabazite (CHA) framework on olefin selectivity during methanol-to-olefin (MTO) and tandem CO_2 hydrogenation was investigated over an aluminosilicate, SSZ-13 and a silicoaluminophospate, SAPO-34 and their bifunctional admixtures with In_2O_3. During MTO, SSZ-13 and SAPO-34 yielded primarily olefins (cumulative selectivity of ~60 % and ~90 %, respectively at cumulative turnover number, TON over 500 mol_C/mol_{H+}). Interestingly, an interpellet admixture of In_2O_3/SSZ-13 (distance between redox sites and BAS of 260–900 μm) predominantly yielded paraffins (cumulative selectivity of ~93 % at cumulative TON over 40) *via* the secondary hydrogenation of olefins as seen from the cumulative paraffin-to-olefin (P/O) ratio of ~21 during CO_2 hydrogenation. In comparison, an interpellet In_2O_3/SAPO-34 admixture yielded majority olefins (cumulative selectivity of ~67 % at cumulative TON over 60) due to a lesser degree of secondary hydrogenation (cumulative P/O ratio of ~0.2) on the BAS in SAPO-34, which has a lower acid strength as compared to SSZ-13. Interestingly, both interpellet admixtures of In_2O_3/SSZ-13 and In_2O_3/SAPO-34 remained stable during tandem CO_2 hydrogenation by favoring the olefin cycle and suppressing the formation of deactivation-inducing-aromatics as probed *via* occluded hydrocarbon analysis, unlike MTO, where SSZ-13 and SAPO-34 showed fast deactivation. However, in intrapellet admixtures (distance between redox sites and BAS of 270–1500 nm) of In_2O_3/SSZ-13 and In_2O_3/SAPO-34, ion exchange of BAS (H^+) with $In^{\delta+}$ (from In_2O_3) inhibited C–C coupling and predominantly formed CH_4. Overall, our study related the product selectivity and deactivation in MTO and tandem CO_2 hydrogenation over CHA framework zeolite/zeotype to the aromatic and olefin cycle propagation in the hydrocarbon pool mechanism. These underpinnings will help with rational catalyst design for tandem CO_2 hydrogenation.

1. Introduction

The tandem thermocatalytic conversion of carbon dioxide (CO_2) into hydrocarbons (HC) through methanol (CH_3OH) intermediate offers a promising route to synthesize potentially carbon–neutral fuels and chemicals and mitigate climate change [1–13]. Recent reports have shown that tandem CO_2 hydrogenation to olefins, and aliphatic and aromatic hydrocarbons were achieved on reducible metal oxide-zeolite admixtures [1,2,9,14–19]. The conversion combines the two steps: (i) CH_3OH synthesis from CO_2 and H_2 over the oxygen vacancies/redox sites of a reducible metal oxide, and (ii) subsequent conversion of CH_3OH to HC *via* the methanol to hydrocarbons (MTH) or methanol to olefins (MTO) over Brønsted acid sites (BAS) of zeolites/zeotypes [3,5,7–9]. The selectivity of HC products predominantly hinges on the latter step due to the shape-selective nature of zeolite/zeotype, which allows the propagation and diffusion of only those molecules that can fit in the pores of the zeolite/zeotype [20–25]. Therefore, the shape-selective property of the zeolite/zeotype is a crucial factor in determining the HC distribution in the tandem CO_2 conversion to HC.

In the micropores of the zeolite, during MTH or MTO, the formation of HC over zeolites/zeotypes proceeds through initiation, propagation, and termination phases [26]. In the initiation phase, dehydrative C–C coupling of CH_3OH over Brønsted acid sites (BAS) of the zeolite/zeotype forms dimethyl ether (DME) and unsaturated HC in the micropores. The unsaturated HCs eventually develop two distinct olefin and aromatic cycles in the propagation phase in a “dual cycle” or “hydrocarbon pool” (HCP) mechanism, as shown in Fig. 1 [25,27–30]. Olefins are believed to undergo methylation and cracking in the olefin cycle, while aromatics are believed to undergo methylation and demethylation in the aromatic cycle [25,31,32]. The two cycles are interconnected *via* the

---

* Corresponding author.
E-mail address: manish.shetty@tamu.edu (M. Shetty).

https://doi.org/10.1016/j.jcat.2024.115518
Received 16 January 2024; Received in revised form 1 April 2024; Accepted 24 April 2024

aromatization of olefins and the dealkylation of aromatics to olefins [33]. The formation of paraffins is proposed to occur *via* a hydrogen transfer (HT) mechanism to maintain the equilibrium between the hydrogen-rich (H-rich) olefin cycle and the hydrogen-lean (H-lean) aromatic cycle [34,35]. The active chain carriers in the HCP eventually form highly unsaturated carbonaceous residues, *i.e.*, polycyclic aromatic hydrocarbons, resulting in the termination of the HC propagation [33,36].

Although the relative propagation of olefin and aromatic cycles largely depends on the shape selectivity of the zeolite/zeotype, when it comes to MTH/MTO, it is just one piece of the puzzle. Several factors, such as the BAS strength of the zeolite/zeotype, the co-presence of H_2 or CO, and the partial pressure of CH_3OH can influence the yield and selectivity of the HCs [33,36–38]. Previous studies by Bhan and co-workers showed that during MTO on CHA framework zeolites/zeotypes with its narrow eight-membered windows (3.8 × 3.8 Å), SSZ-13 an aluminosilicate (*i.e.*, a zeolite) enhanced CH_3OH disproportionation and olefin hydrogenation, thereby increased methane and paraffin selectivity, as compared to SAPO-34, a silicoaluminophosphate (*i.e.*, a zeotype) with weaker acid strength, which showed higher olefin selectivity [38]. Given that the tandem reaction couples CH_3OH synthesis from CO_2 (over a reducible metal oxide) with MTH (over the zeolite/zeotype), how the acid strength of the zeolite/zeotype influences the olefin and aromatic cycles, (Fig. 1), and how that is linked to the HC distribution remains an unexplored question. Furthermore, under the harsh reaction conditions of tandem CO_2 hydrogenation, the migration of elements from the metal oxide to the zeolites has been reported [6,39]. This migration has been shown to lead to the inhibition of MTO/MTH pathway due to the ion exchange of the metal cations with BAS of the zeolite. However, the nature of the interaction of the metal cations with the zeolite/zeotype framework is not well understood.

Previously, Bhan and co-workers demonstrated that increasing the partial pressure of H_2 during MTH suppressed the propagation of the aromatic cycle [36], while increasing the partial pressure of carbon monoxide (CO) and CH_3OH favored the propagation of the aromatic cycle [40–42]. During tandem CO_2 hydrogenation, H_2, CO, and CH_3OH co-exist in the reaction system (unconverted H_2 from CH_3OH synthesis, CO as a side product, and CH_3OH as the main product from the CH_3OH synthesis). However, their combined influence on the "hydrocarbon pool" (HCP) mechanism under the reaction conditions relevant to tandem CO_2 hydrogenation has not been addressed.

Zeolites/zeotypes of chabazite (CHA) topology are known to favor the propagation of the olefin cycle leading to high selectivity towards light olefins by preventing the escape of large aromatic compounds [2,16,17,43–48]. However, a significant drawback of CHA topology is its tendency to deactivate *via* coking, as the active HC chains eventually transform into carbonaceous residues, e.g., polycyclic aromatics, which retain in the pores causing coking [33,36,37,49,50]. However, Sukaran *et al.* demonstrated that during MTO, high-pressure H_2 prevents the formation of polyaromatics *via* the hydrogenation of olefins and aromatics, thus leading to a longer catalyst lifetime [36]. Nevertheless, as unreacted H_2 from CH_3OH synthesis is expected to be present during MTH, how the partial pressure of H_2 influences coking and catalyst lifetime during tandem CO_2 hydrogenation is an interesting question.

This study aims to address the questions on the influence of BAS strength and the presence of H_2, CH_3OH, and CO on the HC distribution and catalyst stability, and their underpinnings in the HCP mechanism. To that end, our objectives are threefold: i) investigate how the acid strength of the zeolite/zeotype affects HC distribution during tandem CO_2 hydrogenation, ii) elucidate how olefin/aromatic cycles propagate with the different BAS strengths in the concurrent presence of H_2, CO, and CH_3OH under tandem reaction conditions, and iii) assess how BAS strength in CHA frameworks influences the catalyst stability. We selected SSZ-13 (Si/Al ratio 7) and SAPO-34 ((Al + P)/Si ratio 7.5) of CHA topology with narrow eight-membered windows (3.8 × 3.8 Å) having similar BAS density, where SSZ-13 has higher BAS strength compared to SAPO-34 [33,38]. We first evaluated the influence of acid strength on MTO in terms of two metrics, propylene-to-ethylene ratio ($C_3^=/C_2^=$) and paraffin-to-olefin (P/O) ratio, which convey the relative propagation of the olefin cycle to the aromatic cycle and the degree of saturation of olefins in HCP, respectively [37]. We then evaluated the influence of BAS strength on HC distribution and catalyst lifetime during tandem CO_2 hydrogenation in two different configurations of bifunctional admixtures of SSZ-13 and SAPO-34 with In_2O_3: interpellet (distance between redox and BAS of 260–900 μm) and intrapellet (distance between redox and BAS of 270–1500 nm). Overall, this study offers

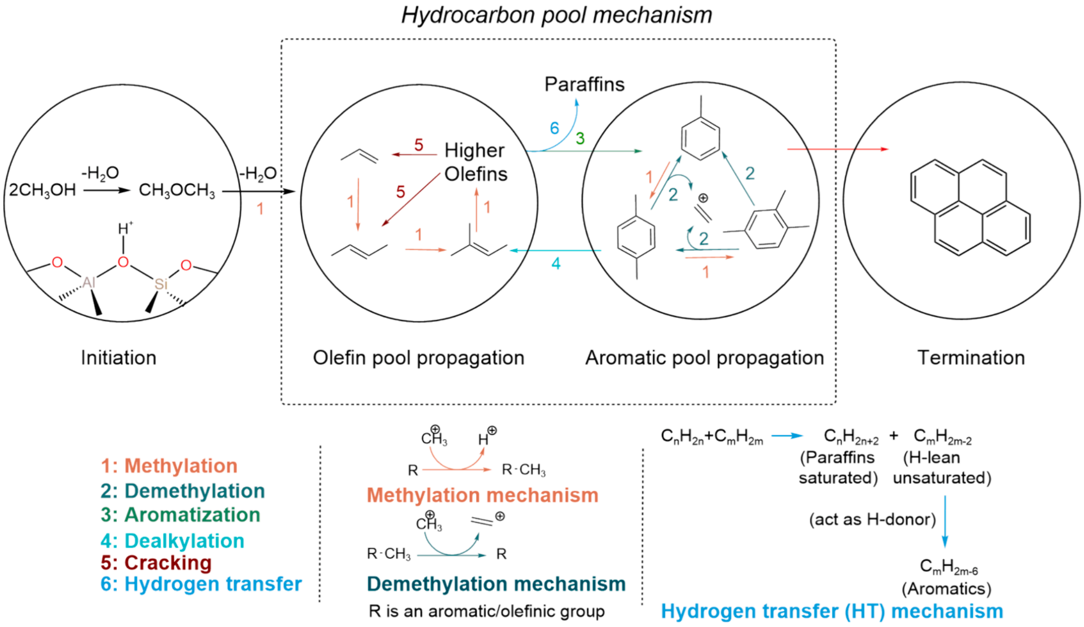

Fig. 1. Hydrocarbon pool (HCP) mechanism of methanol-to-hydrocarbon (MTH) conversion on zeolites/zeotypes including initiation, propagation, and termination phases. The propagation encompasses multiple steps, including olefin methylation, cracking, hydrogen transfer, aromatization, aromatic methylation, and aromatic dealkylation. The competing nature of HCP mechanism determines the selectivity of hydrocarbon products. Adapted with permission from Ilias, S. & Bhan et al [26]. Copyright J. Catal. 2012.

insights into the effect of the acid strength of the CHA framework on the reaction mechanism, HC distribution, and catalyst lifetime, relates the observed catalytic performance to the propagation of aromatic and olefin cycles in the HCP mechanism, and underscores the necessity of rational integration in bifunctional admixtures for efficient tandem CO_2 hydrogenation.

2. Materials and methods

2.1. Materials

Indium (III) nitrate hydrate (99.999 % metal basis, Thermo Scientific chemicals, Richardson, Texas, US) and ammonium hydroxide (28–30 % NH_3 basis, Sigma-Aldrich, St. Louis, Missouri, US) were used to synthesize indium oxide (In_2O_3). Commercial SAPO-34 (SiO_2:Al_2O_3 molar ratio 0.5 with SiO_2 10 wt%, Al_2O_3 42 wt%, and P_2O_5 48 wt%) and SSZ-13 (SiO_2:Al_2O_3 molar ratio 15) were purchased from ACS materials (batch 060922 and MSZ13015, respectively). Sodium nitrate (ReagentPlus, ≥99 %, Sigma Aldrich, St. Louis, Missouri, US) was used for ion-exchange with SSZ-13 and SAPO-34. Fused α-alumina (100–200 mesh, Sigma Aldrich, St. Louis, Missouri, US) was used for spacing in stacked catalyst beds. Methanol (CH_3OH, ≥99.9 %, ACS-grade LC reagent) was purchased from Sigma-Aldrich (St. Louis, Missouri, US) for MTO.

2.2. Synthesis and preparation methods

2.2.1. Synthesis of indium oxide (In_2O_3)

Indium oxide (In_2O_3) was synthesized by the precipitation method [1,6]. Indium (III) nitrate trihydrate ($In(NO_3)_3{\cdot}3H_2O$, 5 g) was dissolved in deionized (DI) water (20 ml). The solution was added dropwise to an ammonium hydroxide (NH_4OH) solution (60 ml, 0.8 M). The as-prepared mixture was aged overnight (12 h, 70 °C) and then filtered under vacuum. The precipitate was washed with ethanol (70 %), dried (5 hr), and calcined (500 °C, 4 h) with air (50 ml/min) in a muffle furnace.

2.2.2. SSZ-13 and SAPO-34

SSZ-13 was calcined (500 °C, 4 h) under air (50 ml/min) in a muffle furnace. SAPO-34 was purchased in calcined (500 °C) form and was used directly. Both were pretreated in the reactor bed in 5 % H_2 (balance N_2) at 300 °C for 1 h and cooled to 40 °C before the reaction.

2.2.3. Preparation of bifunctional In_2O_3/SSZ-13 and In_2O_3/SAPO-34 admixtures

2.2.3.1. Interpellet admixtures (interpellet_In_2O_3/SSZ-13 and interpellet_In_2O_3/SAPO-34). Interpellet admixtures were prepared by physically mixing granules/pellets of In_2O_3 with granules/pellets of SSZ-13 or SAPO-34 at a mass ratio of 1:1 (total 1 g, unless otherwise specified). To prepare the granules/pellets, crystallites of In_2O_3, SSZ-13, and SAPO-34 were separately pressed, crushed, and sieved into 30–60 mesh (size 250–560 μm).

2.2.3.2. Intrapellet admixtures (intrapellet_In_2O_3/SSZ-13 and intrapellet_In_2O_3/SAPO-34). Intrapellet admixtures were prepared by mixing In_2O_3 with SSZ-13 or SAPO-34 crystallites in 1:1 mass ratio in an agate mortar and pestle for 15 min, followed by pressing, crushing, and sieving the mixed powder into granules of 30–60 mesh (size 250–560 μm).

2.2.4. Ion-exchange of SSZ-13 and SAPO-34 with $In^{\delta+}$ (In-SSZ-13 and In-SAPO-34)

In-SSZ-13 (In:Al ratio 3.5:1) and In-SAPO-34 (In:Si ratio 1:1) were prepared by incipient wetness impregnation. For In-SSZ-13, a solution of $In(NO_3)_3{\cdot}3H_2O$ (2 g in 1 ml H_2O) was added dropwise to freshly calcined SSZ-13 (1 g, 500 °C, 4 h). The mixture was then dried (5 hr), and calcined (500 °C, 10 h) with air (50 ml/min) in a muffle furnace. Similarly, for In-SAPO-34, a solution of $In(NO_3)_3{\cdot}3H_2O$ (1.76 g in 1 ml H_2O) was added dropwise to calcined SAPO-34 (3 g, 500 °C, 4 h). The mixture was then dried (5 hr), and calcined (500 °C, 10 h) with air (50 ml/min) in a muffle furnace.

2.2.5. Steam treatment of SSZ-13 (St-SSZ-13)

Steam treatment was conducted over SSZ-13 to create extra framework Al sites (EFAl). Briefly, SSZ-13 (1.5 g) was treated with 0.016 % H_2O in N_2 for 0.5 h, at 400 °C in a stainless steel reactor tube [51]. The characterization and reactivity of steamed SSZ-13 (denoted as St-SSZ-13) is given in the supplementary material Section S1.3.

2.3. Catalytic evaluation

2.3.1. CO_2 hydrogenation

The catalytic conversion of CO_2 hydrogenation was evaluated in a high-pressure tubular stainless steel fixed-bed reactor. The isothermal zone was ensured by using a brass heating block around the reactor tube. Typically, the catalyst (1.0 g, 30–60 mesh) was first pretreated in 5 % H_2 (balance N_2) at 300 °C for 1 h and cooled to 40 °C prior to the reaction. The reaction was conducted at 500 psig and 350 °C, unless otherwise specified. Gas hourly space velocity (GHSV) was calculated using the following equation:

$$\mathrm{GHSV} = \frac{\text{total inlet gas flow rate (ml/h)}}{\text{total mass of the catalyst (g)}} \tag{1}$$

GHSV was maintained at 9000 ml $g_{cat}^{-1}h^{-1}$ with a H_2:CO_2 feed ratio of 3:1 unless otherwise specified.

The products were analyzed by an online gas chromatograph (SRI-GC Multigas 5) equipped with a flame ionization detector (FID), a methanizer (FIDm), and a thermal conductivity detector (TCD). A Haysep D column was connected to the TCD and FIDm for separating and detecting CO_2, CO, CH_4, and C_2-C_4 HC, while the MXT-1 column was connected to the FID for analyzing all HC and oxygenate products (e.g., DME and CH_3OH). The outlet/exhaust from the reactor was further analyzed by Agilent GCMS (8890 GC system and 5977B GC/MSD) equipped with GasPro and HP-5 columns connected to FID and mass spectrometer for further quantification and identification of the products. The product selectivity was calculated on a molar carbon basis. The carbon balance is given on the supplementary material (Table S9).

The CO_2 conversion, selectivity, and space–time-yield (STY) of products were calculated by the following equations:

$$CO_2\ conversion,\ X_{CO_2} = \frac{C_{CO_2,inlet}.F_{inlet} - C_{CO_2,outlet}.F_{outlet}}{C_{CO_2,inlet}.F_{inlet}} \times 100\% \tag{2}$$

where $C_{CO_2,\ inlet}$ and $C_{CO_2,\ outlet}$ are the concentrations of CO_2 at the inlet and outlet, respectively. F_{inlet} and F_{outlet} are the inlet and outlet gas flow rates of the reactor.

$$Selectivity\ of\ C_nH_m\ in\ HC\ distribution = \frac{RRF_{C_nH_m} \times A_{C_nH_m}}{\sum_1^n RRF_{C_nH_m} \times A_{C_nH_m}} \times 100\% \tag{3}$$

$$Selectivity\ of\ CO,\ S_{CO} = \frac{RRF_{CO} \times A_{CO}}{RRF_{CO} \times A_{CO} + RRF_{CH_3OH} \times A_{CH_3OH} + RRF_{DME} \times A_{DME} + \sum_1^n RRF_{C_nH_m} \times A_{C_nH_m}} \times 100\% \tag{4}$$

$$Selectivity\ of\ CH_3OH,\ S_{CH_3OH} = \frac{RRF_{CH_3OH} \times A_{CH_3OH}}{RRF_{CO} \times A_{CO} + RRF_{CH_3OH} \times A_{CH_3OH} + RRF_{DME} \times A_{DME} + \sum_1^n RRF_{C_nH_m} \times A_{C_nH_m}} \times 100\% \tag{5}$$

$$Selectivity\ of\ DME,\ S_{DME} = \frac{RRF_{DME} \times A_{DME}}{RRF_{CO} \times A_{CO} + RRF_{CH_3OH} \times A_{CH_3OH} + RRF_{DME} \times A_{DME} + \sum_1^n RRF_{C_nH_m} \times A_{C_nH_m}} \times 100\% \tag{6}$$

here RRF is the relative response factor and A is the peak area of the species on the chromatogram. The letters n and m denote the number of C and H atoms in C_nH_m. For the catalytic performance evaluation in bar plots, the data was averaged over three points under a specific reaction condition. The carbon balance was done on a carbon mole basis. The carbon balance ranges from 97 % to 104 % as shown in Table S9.

2.3.2. Methanol-to-olefin conversion (MTO)

MTO was conducted in the same tubular stainless steel fixed-bed reactor as in Section 2.3.1. Typically, the catalyst was first pretreated in 5 % H_2 (balance N_2) at 300 °C for 1 h and cooled to 40 °C before the reaction. The reaction was conducted at a pressure of 200 psig and a reaction temperature of 350 °C. CH_3OH was injected using a high-pressure syringe pump (Chemyx Fusion 6000X). Space-time-yield (STY) and cumulative turnover number (TON) for MTO conversion were measured as follows.

$$Space - time\ yield\ (STY)\ of\ C_nH_m = \frac{X_{CH_3OH} \times F_{CH_3OH,inlet} \times \left(1 - \frac{S_{CO}}{100} - \frac{S_{DME}}{100}\right) \times Selectivity\ of\ C_nH_m\ in\ HC\ distribution}{[H^+]} \tag{7}$$

$$STY\ of\ CO = \frac{X_{CH_3OH} \times F_{CH_3OH,inlet} \times \frac{S_{CO}}{100}}{[H^+]} \tag{8}$$

TON was measured by integrating the total STY (sample calculation shown in Table S10) of all products over time as the following equation,

$$Cumulative\ turnover\ number,\ TON = \int_0^t STY\ dt \tag{9}$$

2.4. Catalyst characterization

2.4.1. Powder X-ray Diffraction (PXRD)

The PXRD patterns were acquired using a Rigaku Miniflex II X-ray instrument equipped with Cu-Kα radiation ($\lambda = 1.5406$ Å). The scanning range was set from 5 to 75°, with a step rate of 0.02 and a scan rate of 1°/min. The PXRD patterns of In_2O_3 and bifunctional admixtures were normalized by the In_2O_3 peak at 30.8°, while PXRD patterns for SSZ-13 and SAPO-34 were normalized by the peak at 9.8° and 9.5°, respectively.

2.4.2. Argon physisorption

Surface area measurements were performed using the Anton Paar Autosorb iQ-C-MP EPDM automated gas sorption analyzer. The surface area analysis was carried out using Argon physisorption at 87 K, and the resulting adsorption–desorption isotherms were analyzed using the Brunauer-Emmett-Teller (BET) theory [52]. In summary, a quantity of 10–15 mg of the catalyst was placed in a 6 mm glass cell bulb (without a rod) or a 9 mm glass cell with a rod to reduce void volume. The sample underwent an initial outgassing process at 350 °C for 480 min. Argon physisorption isotherm data were then collected, encompassing 72 adsorption (p/p_o values of $1e^{-6}$ to 0.995) and 27 desorption points (p/p_o values of 0.05–0.995). The isotherm data were subjected to BET analysis, specifically utilizing the adsorption data points ranging from p/p_o values of 0.005–0.3. Total pore volume was calculated based on the assumption that at relative pressures near unity, the pores filled with liquid following the equation below [53]:

$$V_{liq} = \frac{P_a V_{ads} V_m}{RT} \tag{10}$$

The micropore area and volume were calculated using the t-plot method using the deBoer thickness equation (see below) using adsorption data points ranging from p/p_o values of 0.2–0.5. All zeolite-containing samples contained a positive y-intercept on the t-plot indicating the presence of micropores, whereas the bulk In_2O_3 sample's t-plot passed through the origin confirming it to be mesoporous.

$$t = \left[\frac{13.99}{log(P_0/P) + 0.034}\right]^{\frac{1}{2}} \tag{11}$$

The t-plot is a graph of the volume of gas adsorbed at STP (V_{ads}^{STP}) vs the layer thickness (t). The slope of this line (s) is related to the total surface area of the pores given by the equation below. It then follows that the micropore surface area (S_{MP}) is the difference between the BET surface area and S_t.

$$S_t(m^2/g) = \frac{V_{ads}^{STP} \times 15.47}{t} = s \times 15.47 \tag{12}$$

$$S_{MP} = S_{BET} - S_t \tag{13}$$

For samples without micropores, there is good agreement between S_{BET} and S_t (such is the case for bulk In_2O_3). The micropore volume is related to the intercept (i) of this plot given by the following equation.

$$V_{MP} = i \times 0.001547\ (cm^3) \tag{14}$$

Details on BET calculation parameters (slope and intercept) and micropore volume calculations are given in Table S4.

2.4.3. X-ray photoelectron spectroscopy (XPS)

X-ray photoelectron spectroscopy (XPS) measurements were conducted at the Materials Characterization Facility (MCF) located at Texas A&M University, utilizing the EnviroESCA XPS instrument.

The XPS spectra were analyzed using CasaXPS software (version

2.3.16 PR 1.5). Shirley background was selected and the C 1s spectra for adventitious carbon were used for charge correction by assigning the C–C, C–H component binding energy to 284.8 eV (see Table S5 for additional assignments and constraints). Peak deconvolution was done using the Gaussian-Lorentzian (GL30) line shape. The In^{3+} was assigned to 444.03 eV based on the bulk In_2O_3 spectra with a peak splitting placement of 7.54 eV and spin–orbit splitting ratio of 3:2 ($3d_{5/2}$:$3d_{3/2}$) for the In 3d spectrum. In-SSZ-13 and In-SAPO-34 spectra were then fitted with additional components, utilizing the same splitting constraints for In, to account for peak broadening seen with zeolite samples compared to bulk In_2O_3 (Table S6).

2.4.4. *Transmission electron microscopy (TEM)*

Transmission electron microscopy (TEM) analysis was conducted using the FEI TECNAI G2 F20 CRYO FE-TEM instrument, available at the Microscopy and Imaging Center (MIC) situated at Texas A&M University. Before TEM, approximately 5 mg of powder sample was added to 500 mg of isopropanol (IPA, 70 % v/v, Millipore Sigma, Burlington, Massachusetts, US) and sonicated for 2 min in a water bath at room temperature. A drop of the sonicated mixture was then added to a copper grid of 200 mesh (formvar coating thickness 10 nm and carbon coating thickness 1 nm, purchased from Electron Microscopy Sciences) and dried overnight in a dryer at 50 °C.

2.4.5. *Temperature-programmed oxidation (TPO) via thermogravimetric analysis coupled with mass spectrometry (TGA-MS)*

Temperature-programmed oxidation (TPO) of spent catalyst was conducted with TA Instruments Thermogravimetric Analyzer (TGA) Q5000 IR with infrared furnace fed with Ultra-Zero air with 100 μL platinum pans rated to 750 °C (drying phase: 10 °C/min ramp to 120 °C followed by a 15 min isothermal phase, 20 ml/min air. TPO phase: 10 °C/min ramp to 750 °C, followed by a 5 min isothermal phase. Sample weight: ~5–20 mg.) The TGA curve is shown in Fig. S1E and S1F. The exhaust gases from the TGA were connected via a capillary tube to the inlet of a Stanford Research Systems UGA200 Universal Gas Analyzer. Pressure vs. time scans at ~2 s intervals were collected by the UGA during the TPO phase of the TGA regimen.

2.4.6. *Occluded hydrocarbon analysis*

The occluded coke species were analyzed by digesting the spent catalyst. Briefly, 20 mg of spent catalyst was digested in 4 ml of 50 vol% H_2SO_4 aqueous solution and stirred at 60 °C for three days. The organic phase was later extracted using 3 ml of dichloromethane (DCM) containing 0.2 mg of octadecane (C_{18}) as the internal standard. Afterward, 0.5 μL of the organic specimen was injected into the GC–MS (Agilent 8890 GC system and 5977B GC/MSD equipped with an HP-5 column connected to FID and mass spectrometer for further quantification and identification of the products) with the following temperature program: hold for 1 min at 50 °C, then raise the temperature to 250 °C at a rate of 10 °C min^{-1}. The molecules annotated on the chromatograms were identified through fragmentation peak analysis and matching with the NIST database. The product distribution of aromatics was quantified by FID using C_{18} as the internal standard and relative response factors (RRF) for the aromatics.

2.4.7. *Solid-state nuclear magnetic resonance (SSNMR)*

The ^{13}C cross-polarization (CP) and ^{27}Al single-pulse direct nuclear excitation in the presence of high-power 1H decoupling (HPDEC)

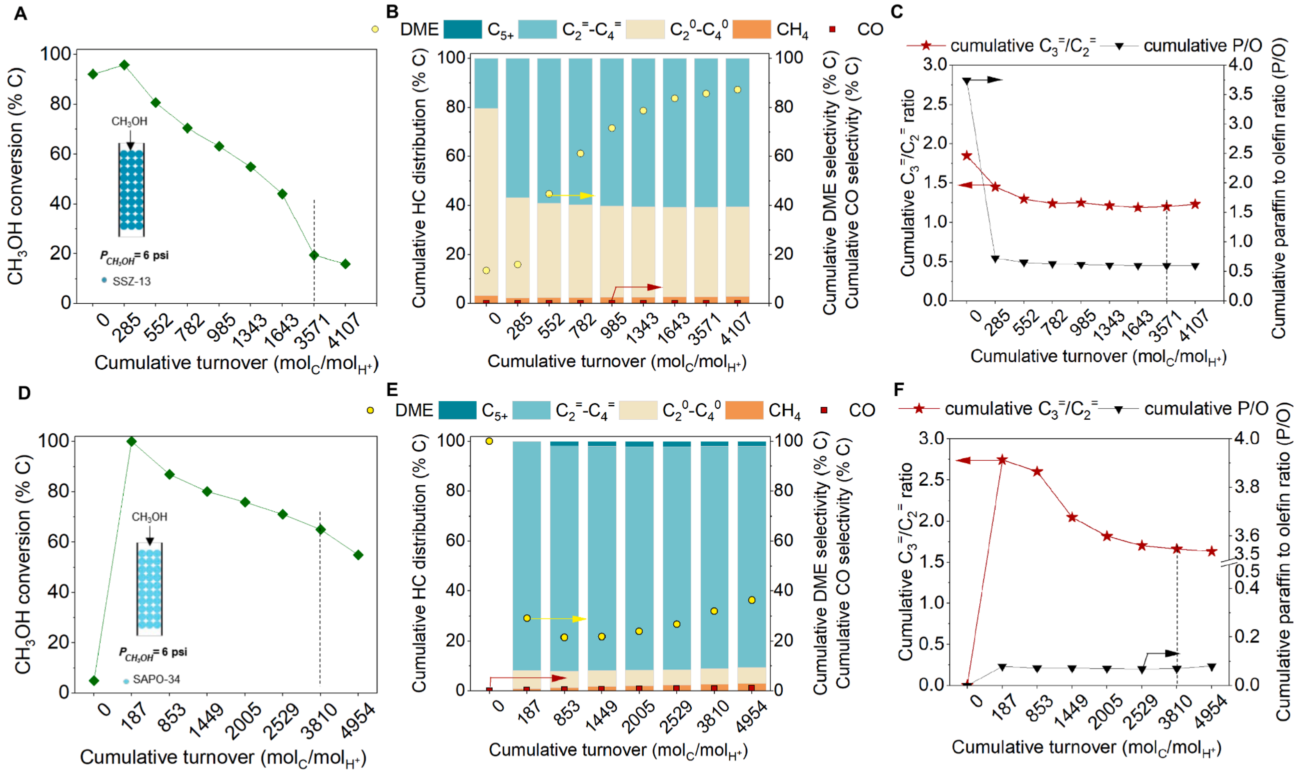

Fig. 2. Effect of the Brønsted acid site (BAS) strength of SSZ-13 and SAPO-34 on methanol-to-olefin (MTO) conversion. (A) CH_3OH conversion with respect to cumulative turnover number (TON) over SSZ-13. (B) Cumulative hydrocarbon (HC) distribution (left axis), DME (right axis), and CO selectivity (right axis) with respect to TON over SSZ-13 during MTO. (C) Cumulative paraffin-to-olefin (P/O) (right axis), and cumulative propylene-to-ethylene ratio ($C_3^=/C_2^=$) (left axis) over SSZ-13 during MTO. Reaction conditions: 350 °C, CH_3OH injection rate 0.006 ml min^{-1}, N_2 flow 75 ml min^{-1}, 0.5 g SSZ-13, total pressure 200 psig with partial pressure of CH_3OH ~6 psig. (D) CH_3OH conversion with respect to TON over SAPO-34 during MTO conversion. (E) Cumulative HC distribution (left axis), DME (right axis), and CO selectivity (right axis) with respect to TON over SAPO-34 during MTO. (F) Cumulative P/O (right axis), and cumulative $C_3^=/C_2^=$ ratio (left axis) over SAPO-34 during MTO. Reaction conditions: 350 °C, CH_3OH injection rate 0.006 ml min^{-1}, N_2 flow 75 ml min^{-1}, 0.5 g SAPO-34, total pressure 200 psig with partial pressure of CH_3OH ~6 psig.

experiments were carried out with a Bruker Avance-NEO solid-state NMR spectrometer (400 MHz for 1H nuclei) equipped with a standard two-channel 4 mm MAS probe head. The external references were tetramethylsilane (TMS) and Al_2O_3 for ^{13}C and ^{27}Al nuclei, respectively. The CP time for the ^{13}C NMR experiments was 1.2 ms. Approximately 50 mg sample was used for SSNMR.

2.4.8. *Ammonia temperature programmed desorption (NH_3-TPD)*

Ammonia temperature programmed desorption (NH_3-TPD) was performed for SSZ-13, SAPO-34, In-SSZ-13 and In-SAPO-34. Briefly, 50 mg sample was calcined with air (400 °C, 3 h) and cooled down to 100 °C. A flow of 5 % NH_3 (2.5 ml min^{-1} NH_3 and 47.5 ml min^{-1} N_2) was introduced to the sample, followed by a purge with 50 ml min^{-1} N_2 at 100 °C to remove any physiosorbed NH_3. The sample was then heated up to 600 °C with a 10 °C min^{-1} ramp rate under 50 ml min^{-1} N_2 flow, followed by an isothermal holdup of 2 h [51].

3. Result and discussion

3.1. *Influence of Brønsted acid site (BAS) strength on the hydrocarbon pool (HCP) mechanism for methanol-to-olefins (MTO) conversion*

To assess the influence of BAS strength on HCP mechanism (Fig. 1), we first employed SSZ-13 (Si/Al ratio 7) and SAPO-34 ((Al + P)/Si ratio 7.5) for MTO at 350 ℃ and partial pressure of CH_3OH (p_{CH_3OH}) of ~6 psig (CH_3OH injection rate 0.006 ml min^{-1}, N_2 flow 75 ml min^{-1}, 0.5 g SSZ-13 (or SAPO-34), total pressure 200 psig). The stability of SSZ-13 and SAPO-34 was assessed by calculating the cumulative turnover number (TON), which is defined as the total amount of CH_3OH-derived carbon atoms observed in the effluent products normalized by the total BAS in the catalyst. We used TON instead of conversion over time-on-stream (TOS), as it accurately represents the catalytic history of the catalyst by indicating how many moles of CH_3OH were turned into products per mole BAS [54].

Fig. 2A shows that during MTO, SSZ-13 underwent rapid deactivation with CH_3OH conversion decreasing from 92 % to 16 % with increasing TON from ~0 to 4107 mol_C/mol_{H+}. Further, the cumulative HC distribution (shown in Fig. 2B) shows that at low TON (0.03 mol_C/mol_{H+}), the formation of paraffins (77 % among HC), mainly propane (67 % in HC distribution see Table S13), was favored. Consistent with our observations, Davis and co-workers have reported that SSZ-13 with a low Si/Al ratio (<20) promotes the formation of propane and aromatics during the initial transient period of MTO *via* hydrogen-transfer (HT) mechanism that connects the olefin and aromatic cycles in HCP mechanism, which also causes deactivation by coking [55]. Additionally, similar HT transfer could also be promoted by Lewis acid sites (LAS) which likely favor paraffin formation by propagating the aromatic cycle (see Fig. S10). However, Fig. 2B demonstrates that the HC distribution eventually stabilized after a TON of 285 mol_C/mol_{H+} with 2 % CH_4, ~37.5 % paraffins (C_2^0–C_4^0), ~60.5 % lower olefins ($C_2^=$-$C_4^=$), and no longer-chain HCs (C_{5+}), as the pools mature. Consistent with literature, Fig. 2B further demonstrates that the selectivity of dimethyl ether (DME) increased after a TON of 285 mol_C/mol_{H+}, likely due to the deactivation of SSZ-13 reducing the secondary conversion of DME to HC [33].

We further assessed the catalytic performance of SSZ-13 in terms of two parameters, (i) cumulative paraffin-to-olefin (P/O) ratio, which indicates the degree of saturation of olefins in HCP, and (ii) cumulative propylene-to-ethylene ($C_3^=/C_2^=$) ratio, which indicates the relative propagation of olefin to aromatic cycle as propylene predominantly comes from the olefin cycle [26], and ethylene is exclusively the terminal product from the aromatic cycle [40]. The cumulative $C_3^=/C_2^=$ ratio decreased with increasing TON over SSZ-13, eventually stabilizing at a value of 1.25 when the cumulative TON reached 782 mol_C/mol_{H+}, as shown in Fig. 2C [41]. The decreasing trend in cumulative $C_3^=/C_2^=$ ratio with increasing TON indicates that the propagation of the olefin cycle was suppressed at higher TON likely *via* olefin aromatization to favor the aromatic cycle, which is further evident from the fast initial deactivation shown in Fig. 2A [38]. Additionally, as the HCP matured after a TON of 285 mol_C/mol_{H+}, the cumulative P/O ratio stayed at a similar value of ~0.6 (see Fig. 2C).

Similar to SSZ-13, SAPO-34 underwent deactivation during MTO, with CH_3OH conversion decreasing from 100 % to 56 % with increasing TON from ~0 to 4954 mol_C/mol_{H+} (see Fig. 2D). However, at a similar TON of ~3600 mol_C/mol_{H+}, CH_3OH conversion over SAPO-34 (65 %) was higher as compared to SSZ-13 (19 %), as shown in Fig. 2A, and 2D, respectively, indicating faster deactivation of SSZ-13 (compared to SAPO-34) likely *via* the formation of polycyclic species [38]. This is further evident from the higher deactivation rate constants (0.8 h^{-1} over SSZ-13, as compared to 0.06 h^{-1} over SAPO-34, shown in Fig. S1C and S1D, respectively) and coke formation over SSZ-13 (0.3 $g_{coke}/g_{SSZ\text{-}13}$, as compared to 0.24 $g_{coke}/g_{SAPO\text{-}34}$ after a TOS of 40 h, as shown in Fig. S1E and S1F, respectively), as compared to SAPO-34 (Fig. S1D and S1F). The slower deactivation of SAPO-34 over SSZ-13 was likely due to its lower BAS strength.

Additionally, similar to SSZ-13, the cumulative $C_3^=/C_2^=$ ratio decreased from 2.74 to 1.63 as the TON increased from ~187 to 3801 mol_C/mol_{H+} over SAPO-34, indicating that the aromatic cycle propagates more as SAPO-34 deactivates with increasing TON. However, at a similar TON of ~3600 mol_C/mol_{H+}, the cumulative $C_3^=/C_2^=$ ratio was lower over SSZ-13 (~1.25) than SAPO-34 (~1.66), indicating that the aromatic cycle was propagated more over SSZ-13 with its higher BAS strength, consistent with the higher deactivation rate constants and higher coke formation over SSZ-13 (shown in Fig. S1C, S1E).

Furthermore, the HC distribution (see Fig. 2E) over SAPO-34 eventually stabilized after a TON of 1449 mol_C/mol_{H+} with ~2 % CH_4, ~6% C_2^0-C_4^0, ~90 % $C_2^=$-$C_4^=$, and ~2 % C_{5+}. As there were ~8 % paraffins in HC distribution (compared to ~40 % for SSZ-13), the formation of paraffins *via* hydrogen-transfer (HT) connecting the aromatic and olefins cycles over SAPO-34 was likely less favored [36]. This was further evident from the low value of cumulative P/O ratio of 0.07 (after a TON of 1449 mol_C/mol_{H+}) over SAPO-34 in Fig. 2F compared to cumulative P/O ratio of 0.6 over SSZ-13 at a similar TON of 1343 mol_C/mol_{H+} in Fig. 2C.

Taken together, compared to SAPO-34, SSZ-13 deactivated faster and showed lower conversion of CH_3OH at similar TON. Additionally, SSZ-13 yielded a higher degree of saturation (cumulative P/O ratio of 0.6) due to its higher acid strength, as compared to SAPO-34 (cumulative P/O ratio of 0.07) (Fig. 2C and F). Furthermore, with increasing TON, the cumulative $C_3^=/C_2^=$ ratio dropped over SSZ-13 and SAPO-34, showing that the propagation of the aromatic cycle was favored with increasing TON, which further led to the deactivation of the catalyst *via* coking.

We further performed occluded HC analysis to identify the coke species formed over SSZ-13 and SAPO-34 during MTO. Fig. 3A and B show the chromatograms of the aromatic species formed over SSZ-13 and SAPO-34, respectively, identified by GCMS. The product distribution of aromatics revealed that both SSZ-13 and SAPO-34 had similar distributions of naphthalenes, anthracenes, and pyrenes, as shown in Fig. 3C. We further conducted solid-state ^{13}C NMR of spent SSZ-13 and SAPO-34 (see Fig. 3D). Peaks at a chemical shift of 15–25 ppm are considered to be R-CH_3 or R-CH_2-R groups in the form of alkyl groups attached to aromatics, whereas the peaks at 125–135 ppm are assigned to both alkylated and non-alkylated aromatics [56]. As shown in Fig. 3D, the ratio of peak areas for aromatics to alkyl groups was higher over SSZ-13 ($A_{aromatic}/A_{alkyl} = 4.9$), as compared to SAPO-34 ($A_{aromatic}/A_{alkyl} = 2.1$), indicating more aromatics formation over SSZ-13 during MTO. This observation aligns with the higher deactivation rate constants (0.8 h^{-1} over SSZ-13, as compared to 0.06 h^{-1} over SAPO-34, shown in Fig. S1C and S1D, respectively) and higher amount of coke formation over SSZ-13 (0.3 $g_{coke}/g_{SSZ\text{-}13}$, as compared to 0.24 $g_{coke}/g_{SAPO\text{-}34}$ after a TOS of 40 h, as shown in Fig. S1E and S1F, respectively) during MTO.

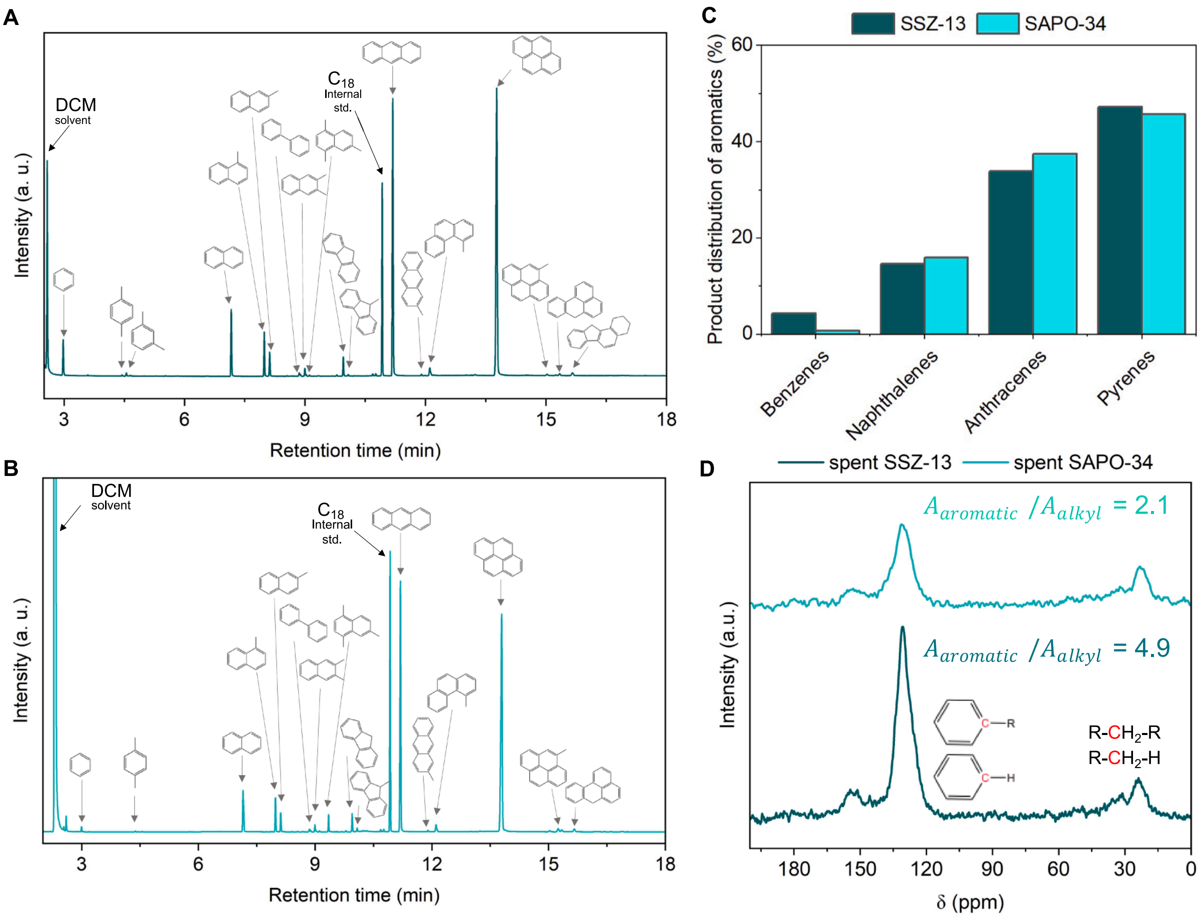

Fig. 3. Identification of coke species formed over SSZ-13 and SAPO-34 during MTO. (A) Chromatogram by gas chromatograph and mass spectrometer (GCMS) for occluded aromatics in spent SSZ-13. (B) Chromatogram by GCMS for occluded aromatics in spent SAPO-34. (C) Aromatic distribution of coke species formed over SSZ-13 and SAPO-34. (D) Solid-state ^{13}C nuclear magnetic resonance (SSNMR) spectra conducted over spent SSZ-13 and SAPO-34.

3.2. Influence of Brønsted acid site (BAS) strength during tandem hydrogenation of CO_2

SSZ-13 and SAPO-34, when used individually, do not display any catalytic activity for CO_2 hydrogenation as the tandem reaction necessitates bifunctionality for CH_3OH synthesis and MTO [7,57]. To address this, we selected In_2O_3 as the CH_3OH synthesis catalyst (which forms only C_1 products: 6.3 % CH_3OH, 1.9 % CH_4, and 91.8 % CO during CO_2 hydrogenation at 350 °C, 500 psig, 9000 ml $g_{cat}^{-1}h^{-1}$, H_2:CO_2 ratio 3:1, as shown in Fig. 4A) and evaluated the influence of BAS strength in zeolite/zeotype on CO_2 hydrogenation by combining SSZ-13 and SAPO-34 with In_2O_3 in bifunctional admixtures. We evaluated two configurations of admixtures with varying distances between the redox sites of In_2O_3 and BAS of SSZ-13 and SAPO-34 (estimated computationally as described in supplementary material Section S3). For interpellet and intrapellet admixtures, the distances were between 260–914 µm and 270–1500 nm, respectively (see Table S7). Stacked bed configurations, where the redox sites of In_2O_3 and BAS of SSZ-13 and SAPO-34 are in milliscale range (3–10 mm), were not employed due to the inefficient transfer of intermediate CH_3OH during the tandem reaction (see Fig. S6), as reported in our previous study [24,57].

3.2.1. Interpellet admixture

Interpellet admixture of In_2O_3 and SSZ-13, henceforth denoted as interpellet_In_2O_3/SSZ-13, showed 24 % CO_2 conversion with a CO selectivity of ~78 % (formed *via* reverse water gas shift, RWGS over In_2O_3) and a HC distribution with ~3.5 % CH_4, ~93 % C_2^0-C_4^0 and ~3.5 % $C_2^=$-$C_4^=$ (Fig. 4A). Among the paraffins, the propane selectivity was 77 % (see Table S11), which makes interpellet_In_2O_3/SSZ-13 a great system to convert CO_2 to liquified petroleum gas (LPG). Interestingly, the interpellet admixture of In_2O_3 and SAPO-34, henceforth denoted as interpellet_In_2O_3/SAPO-34, exhibited a 26.8 % CO_2 conversion with a CO selectivity of ~95 % and a HC distribution with ~32.9 % CH_4, ~7.2 % C_2^0-C_4^0 and ~59.9 % $C_2^=$-$C_4^=$. Therefore, interpellet_In_2O_3/SAPO-34 favored the formation of olefins, contrary to interpellet_In_2O_3/SSZ-13. We infer that the difference in the catalytic performance of interpellet_In_2O_3/SSZ-13 and interpellet_In_2O_3/SAPO-34 could be attributed to the difference in the strength of BAS in SSZ-13 and SAPO-34, where the higher acid strength of SSZ-13 likely promoted the formation of paraffins by the hydrogenation of olefins in the presence of H_2 *(vide infra)* [36].

We further evaluated the time-averaged combined space–time yield (STY) of HC and CH_3OH + DME (presuming all HCs form *via* CH_3OH intermediate) over interpellet_In_2O_3/SSZ-13 and interpellet_In_2O_3/SAPO-34 at 350 °C, 500 psig, 9000 ml $g_{cat}^{-1}h^{-1}$, H_2:CO_2 ratio 3:1, In_2O_3:SSZ-13 (or SAPO-34) mass ratio 1:1, as shown in Fig. 4B. Interpellet_In_2O_3/SSZ-13 exhibited STY of 9.9 × 10^{-5} mol_C g_{cat}^{-1} min^{-1}, whereas interpellet_In_2O_3/SAPO-34 yielded 3.3 × 10^{-5} mol_C g_{cat}^{-1} min^{-1}. Furthermore, we observed some unconverted CH_3OH over SAPO-34 (~1.5 × 10^{-5} mol_C g_{cat}^{-1} min^{-1}) and no unconverted CH_3OH over SSZ-13 (see Fig. 4B). We infer that the complete conversion of intermediate CH_3OH over SSZ-13 during tandem reaction likely shifted the CH_3OH synthesis equilibrium forward over In_2O_3 and suppressed the side reactions of RWGS and methanation [24,59], thereby exhibiting less selectivity of CO and CH_4 due to the higher acid strength of SSZ-13, as compared to SAPO-34. Therefore, the higher acid strength of SSZ-13

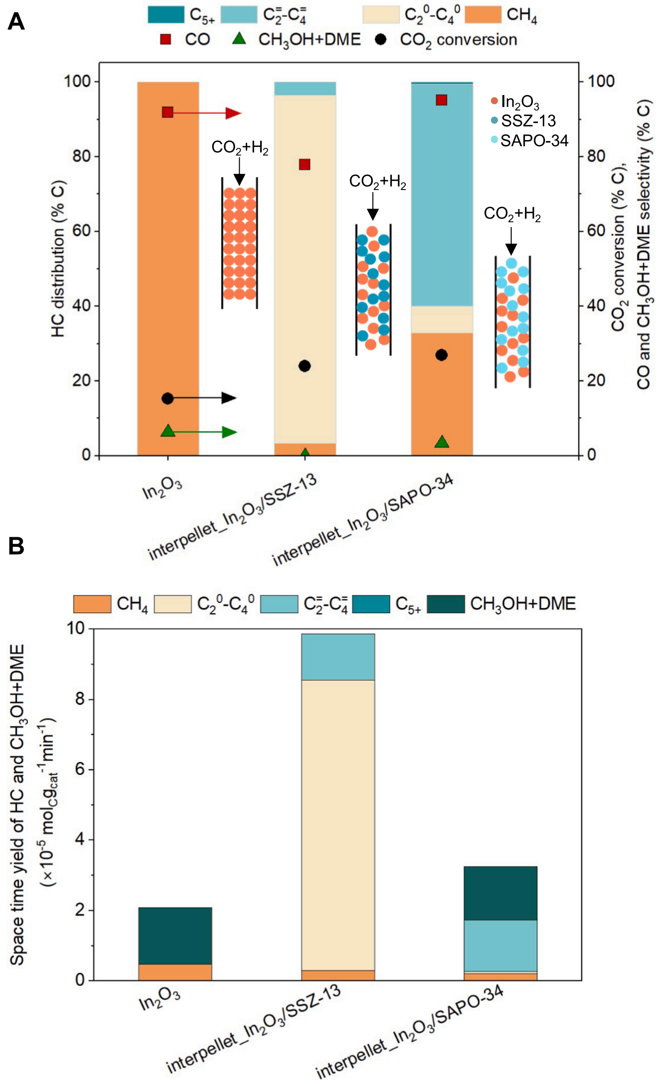

Fig. 4. Requirement of dual functionalities for tandem hydrogenation of CO_2. A) Catalytic performance of In_2O_3, interpellet_In_2O_3/SSZ-13, and interpellet_In_2O_3/SAPO-34 during CO_2 hydrogenation. The left axis shows HC distribution, and the right axis shows CO_2 conversion, CO, and CH_3OH + DME selectivity. B) Space-time yield (STY) of HC and CH_3OH + DME over In_2O_3, interpellet_In_2O_3/SSZ-13, and interpellet_In_2O_3/SAPO-34 during CO_2 hydrogenation. Reaction conditions: 350 °C, 500 psig, 9000 ml $g_{cat}^{-1}h^{-1}$, H_2:CO_2 ratio 3:1, In_2O_3:SSZ-13 (or SAPO-34) mass ratio 1:1. All values were time-averaged during the entire time-on-stream. The catalyst showed limited deactivation after an initial induction zone.

likely has a higher CH_3OH conversion capacity, yielding STY of CH_3OH ~0 $mol_C\ g_{cat}^{-1}\ min^{-1}$, as compared to SAPO-34. Nonetheless, both interpellet_In_2O_3/SSZ-13 and interpellet_In_2O_3/SAPO-34 had higher STY than In_2O_3 alone (2.0 × 10^{-5} $mol_C g_{cat}^{-1} min^{-1}$), implying that both SSZ-13 and SAPO-34 caused a forward shift in the CH_3OH synthesis equilibrium (equilibrium limited at 350 °C) *via* MTO (*per Le Chatelier* principle), consequently driving the overall CO_2 conversion and combined STY [5,58].

To analyze the differences in the HC distribution, product selectivity, and STY, the influence of BAS strength on HCP during tandem CO_2 hydrogenation was further evaluated for interpellet_In_2O_3/SSZ-13 and interpellet_In_2O_3/SAPO-34 by analyzing the CO_2 conversion, cumulative HC distribution, cumulative P/O ratio, and cumulative C_3/C_2 ratio with increasing cumulative TON. CO_2 conversion over interpellet_In_2O_3/SSZ-13 remained constant at ~27 % with increasing TON as shown in Fig. 5A. Further, with increasing TON, the cumulative HC distribution was stable with ~3.3 % CH_4, ~92.2 % C_2^0-C_4^0, and ~4.5 % $C_2^=$-$C_4^=$, and CO selectivity of ~80 %. This indicates the deactivation of SSZ-13 was greatly reduced during tandem CO_2 hydrogenation (as compared to MTO shown in Fig. 2A). We further evaluated cumulative C_3 (propane + propylene) /C_2 (ethane + ethylene) and P/O ratio. We note that olefins undergo saturation in the presence of H_2 [36], therefore, we considered the cumulative C_3/C_2 ratio rather than cumulative $C_3^=/C_2^=$ ratio to holistically quantify the propylene and ethylene coming out of olefin and aromatic cycles, respectively, in the presence of H_2. Over interpellet_In_2O_3/SSZ-13, cumulative C_3 /C_2 ratio was ~15.5 at a TON of 1338 mol_C/mol_{H+}, which was ~12 × higher than for MTO alone over SSZ-13 (~1.3 at TON of 1343 mol_C/mol_{H+} in Fig. S2C). We infer that the increased cumulative C_3/C_2 ratio during tandem hydrogenation could be attributed to the presence of unreacted H_2 favoring the propagation of the olefin cycle. Previously, Bhan and co-workers reported that HCHO produced *via* CH_3OH disproportionation reacts with olefins at BAS to form dienes *via* Prins condensation, which reacts stepwise to form H-lean aromatics (leading to higher $C_2^=$ formation from the aromatic cycle) [36,41,60]. However, under tandem hydrogenation conditions, H_2 likely promotes the saturation of the olefins, thereby interrupting the formaldehyde (HCHO)-mediated transformation of olefins to aromatics through Prins condensation [36]. This was supported by the increased cumulative P/O ratio over interpellet_In_2O_3/SSZ-13, showing a value of ~21 at TON of 1343 mol_C/mol_{H+}, which is ~35 × higher than for MTO over SSZ-13 (~0.6 at TON of 1343 mol_C/mol_{H+} in Fig. 2C).

Similar to interpellet_In_2O_3/SSZ-13, CO_2 conversion over interpellet_In_2O_3/SAPO-34 remained steady at ~26 % with increasing TON as shown in Fig. 5D. The cumulative HC distribution was stable after a TON of 540 mol_C/mol_{H+} with ~16 % CH_4, ~17 % C_2^0-C_4^0, and ~67 % $C_2^=$-$C_4^=$. The steady CO_2 conversion and HC distribution indicate that SAPO-34 remained stable during CO_2 hydrogenation, *akin* to SSZ-13. However, the cumulative P/O ratio of ~0.2 after TON of 1503 mol_C/mol_{H+} (Fig. 5F) indicates that the degree of olefin saturation over SAPO-34 was lower compared to SSZ-13 (~21 at TON of 1338 mol_C/mol_H in Fig. 5C for SSZ-13), likely due to its lower BAS strength. Interestingly, the cumulative C_3/C_2 ratio was found to be lower (~3 at TON of 1503 mol_C/mol_{H+}) compared to SSZ-13 (~15.5 at TON of 1338 mol_C/mol_H in Fig. 5C), indicating that the propagation of olefin cycle is less favored over SAPO-34 than SSZ-13 during CO_2 hydrogenation. Nonetheless for both SSZ-13 and SAPO-34, their deactivation in interpellet admixtures was hindered during CO_2 hydrogenation, as compared to MTO.

The cumulative P/O ratio was found to be higher for SSZ-13 than SAPO-34, in line with the higher BAS strength of SSZ-13. A higher cumulative P/O could be caused by two factors during CO_2 hydrogenation: (i) the HT mechanism where the formation of H-lean aromatics causes the formation of a stoichiometric amount of paraffins to maintain the equilibrium of the dual cycle mechanism during MTO (see Fig. 1), subsequently enhancing P/O ratio and decreasing C_3/C_2 (e.g. interestingly such trend was observed for steamed SSZ-13 where LAS likely promoted aromatic cycle propagation, as shown in Fig. S11), and/or (ii) secondary hydrogenation of olefins to paraffins in the presence of H_2. If the higher P/O ratio on SSZ-13 was solely the result of the HT mechanism, the cumulative C_3/C_2 ratio would concomitantly be lower for SSZ-13 compared to MTO. However, a higher cumulative C_3/C_2 ratio was observed over SSZ-13, suggesting that this may not be caused solely *via* HT. Therefore, we can infer that the high cumulative P/O ratio in interpellet_In_2O_3/SSZ-13, as compared to interpellet_In_2O_3/SAPO-34, is the result of the higher extent of secondary hydrogenation of olefins to paraffins in the presence of H_2, likely due to its higher acid strength.

3.2.1.1. *Influence of partial pressure of H_2 on hydrocarbon pool (HCP) mechanism.*

To probe whether the higher degree of saturation of olefins during tandem CO_2 hydrogenation was caused by secondary

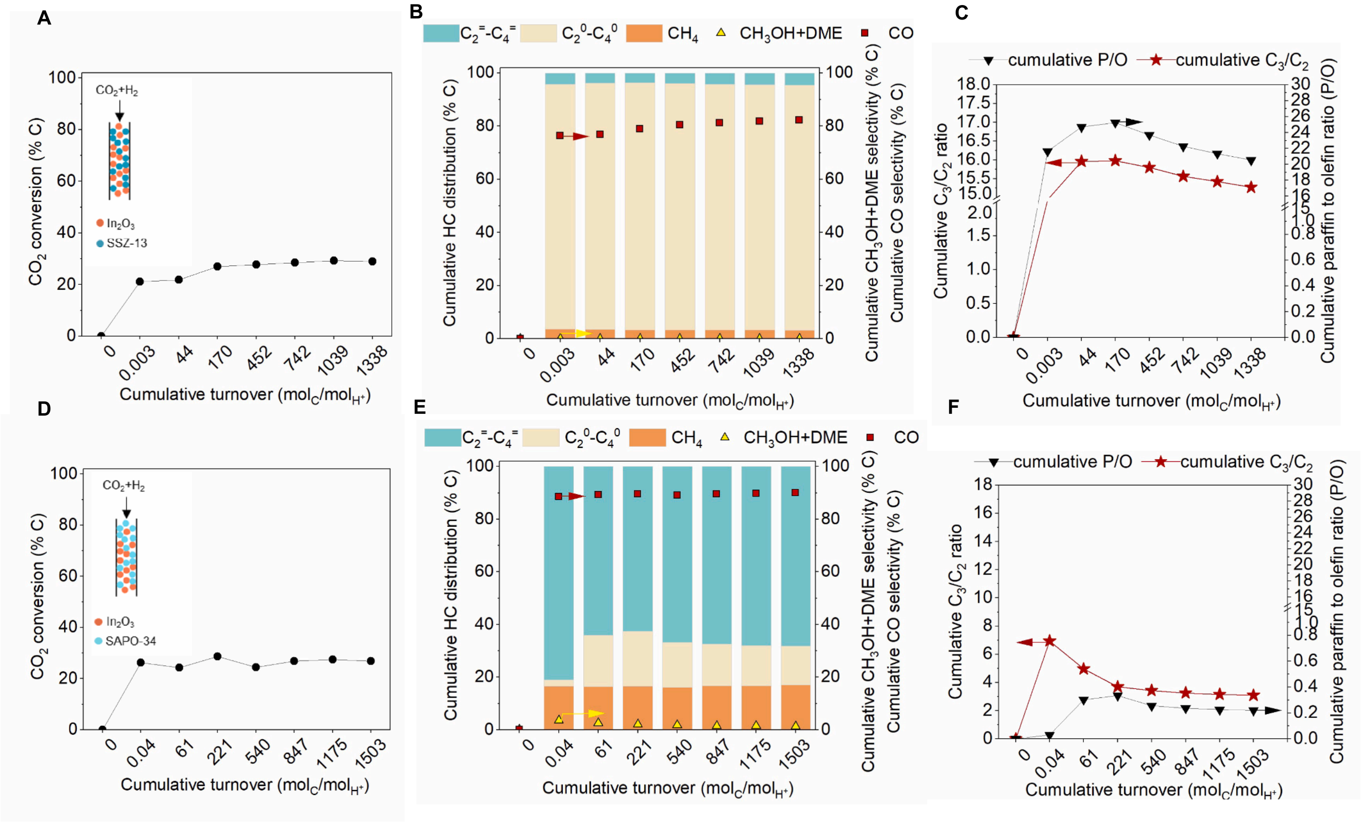

Fig. 5. Influence of acid strength of chabazite (CHA) framework on catalytic performance during tandem hydrogenation of CO_2. (A) CO_2 conversion on interpellet_In_2O_3/SSZ-13 with respect to cumulative turnover number (TON). (B) Cumulative hydrocarbon (HC) distribution (left axis), CH_3OH + DME (right axis), and CO selectivity (right axis) over interpellet_In_2O_3/SSZ-13. (C) Cumulative paraffin-to-olefin (P/O) (right axis), and cumulative C_3(propane and propylene)-to-C_2(ethane and ethylene) ratio (left axis) over interpellet_In_2O_3/SSZ-13. (D) CO_2 conversion on interpellet_In_2O_3/SAPO-34 with respect to TON. (E) HC distribution (left axis), CH_3OH + DME (right axis), and CO selectivity (right axis) over interpellet_In_2O_3/SAPO-34 during CO_2 hydrogenation. (F) Cumulative P/O (right axis), and cumulative C_3/C_2 ratio (left axis) over interpellet_In_2O_3/SAPO-34 during CO_2 hydrogenation. Reaction conditions: 350 °C, 500 psig, 9000 ml $g_{cat}^{-1}h^{-1}$, H_2:CO_2 ratio 3:1, In_2O_3:SSZ-13 (or SAPO-34) mass ratio 1:1.

hydrogenation, we evaluated MTO over SSZ-13 and SAPO-34 in the presence of H_2 as shown in Fig. 6 at 350 °C. Over SSZ-13, CH_3OH conversion remained at ~96 % as the cumulative TON increased from 281 to 2659 mol_C/mol_{H+}, while over SAPO-34, CH_3OH conversion decreased from 100 % to 82 % with increasing TON from 328 to 2984 mol_C/mol_{H+}. Consistent with previous reports, in both cases, the observed deactivation was lesser compared to MTO without H_2 (see Fig. 2A and 2D) [36]. Additionally, for SSZ-13, the cumulative C_3/C_2 ratio was found to be ~7 at a TON of 1474 mol_C/mol_{H+} during MTO with H_2 (see Fig. 6C), which was higher than the cumulative C_3/C_2 (~1.3 at a TON of 1343 mol_C/mol_{H+}) observed for MTO without H_2 in Fig. S2C, indicating olefin cycle propagation was more favored in the presence of H_2. Interestingly, HC distribution showed increased paraffin selectivity of ~78 % (at 1474 mol_C/mol_{H+}), which was also higher than MTO (~37.5 % in Fig. 2B at 1343 mol_C/mol_{H+}). This was further reflected in the cumulative P/O ratio which was found to be ~22 × higher in the presence of H_2 (~13 at 1474 mol_C/mol_{H+} in Fig. 6C, as compared to 0.6 at 1343 mol_C/mol_{H+} in Fig. 2C).

We infer that the higher amount of paraffin in the presence of H_2 was not largely formed *via* HT to balance between the H-rich olefin cycle and H-lean aromatic cycle (as shown in Fig. 1), as the propagation of the aromatic cycle is hindered for SSZ-13 (as evident from increased cumulative C_3/C_2 ratio in Fig. 6C and low deactivation in Fig. 6A). Rather, paraffins are predominantly formed *via* the secondary hydrogenation of olefins over BAS of SSZ-13 in the presence of H_2. It is further to be noted that some amount of CO (~20 %) was formed over SSZ-13 and SAPO-34 during MTO with H_2 (Fig. 6B and E, respectively). We infer that CO was likely formed *via* the disproportionation/decarbonylation of HCHO [33,61], rather than the disproportionation of CH_3OH as our control experiment showed no CO formation during MTO with H_2 co-feed without any catalyst (under reaction conditions of 350 ℃, CH_3OH injection rate 0.006 ml min^{-1}, H_2:N_2 ratio 3:1 with a total flow of 75 ml min^{-1}, total pressure 200 psig with partial pressure of CH_3OH ~6 psig). Although we did not observe HCHO in products, Wei *et al.* and Dewaele *et al.* observed HCHO at lower CH_3OH conversion, formed *via* CH_3OH disproportionation, which aids in HCHO-mediated olefin aromatization [62–64]. Bhan and co-workers reported that during MTO, HCHO reacts with olefins at BAS to form dienes *via* Prins condensation, which reacts stepwise to form H-lean aromatics [36,41,60]. Therefore, the removal of HCHO in the presence of H_2 could further contribute to the inhibition of olefin aromatization [33,61]. Taken together, the secondary hydrogenation of olefins to paraffins and the removal of HCHO by H_2 likely suppressed olefin aromatization, thereby favoring the olefin cycle over SSZ-13 in the presence of H_2 [36].

The enhanced propagation of the olefin cycle during MTO in the presence of H_2 can also be inferred for SAPO-34, where the cumulative C_3/C_2 ratio was 3.5 at a TON of 1041 mol_C/mol_{H+} (see Fig. 6F), compared to 2.6 at 853 mol_C/mol_{H+} during MTO in Fig. S2D. The cumulative P/O ratio was found to increase by ~7.5 × in the presence of H_2 (0.6 at 1041 mol_C/mol_{H+} in Fig. 6F, as compared to 0.08 at 853 mol_C/mol_{H+} in Fig. 2F).

In sum, the presence of the H_2 co-feed likely suppressed the aromatic cycle propagation during MTO, which in turn reduced the deactivation of SSZ-13 and SAPO-34 by inhibiting the formation of deactivation-inducing polycyclic aromatics (Fig. 6A, D). With less propagation of the aromatic cycle, the formation of paraffins *via* HT is expected to be

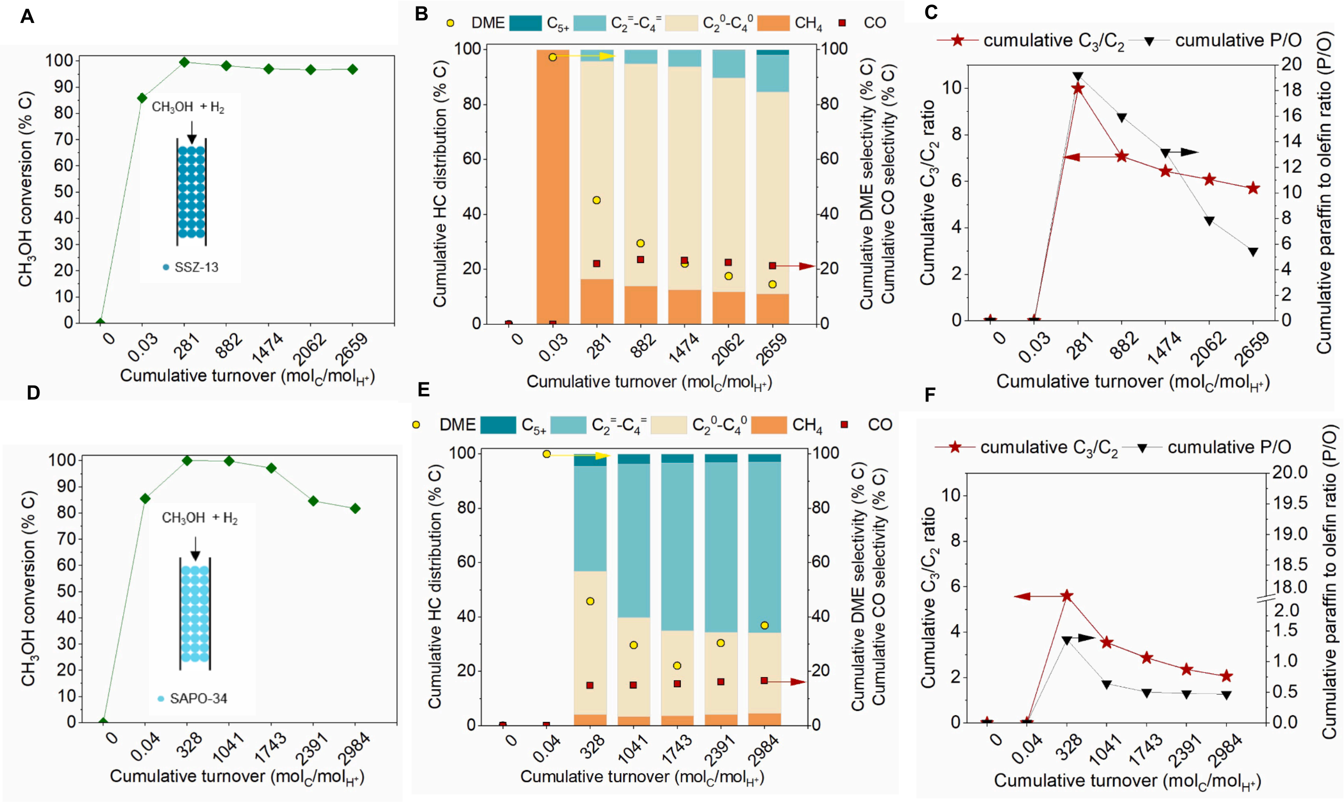

Fig. 6. Effect of H_2 co-feed on MTO conversion. (A) CH_3OH conversion with respect to cumulative turnover number (TON) over SSZ-13. (B) Cumulative hydrocarbon (HC) distribution (left axis), DME (right axis), and CO selectivity (right axis) over SSZ-13. (C) Cumulative paraffin-to-olefin (P/O) (right axis), and cumulative C_3 (propane and propylene)-to-C_2 (ethane and ethylene) ratio (left axis) over SSZ-13 during MTO with H_2 co-feed. (D) CH_3OH conversion with respect to TON over SAPO-34. (E) Cumulative HC distribution (left axis), DME (right axis), and CO selectivity (right axis) over SAPO-34. (F) Cumulative P/O (right axis), and cumulative C_3/C_2 ratio (left axis) over SAPO-34 during MTO with H_2 co-feed. Reaction conditions: 350 °C, CH_3OH injection rate 0.006 ml min^{-1}, H_2:N_2 ratio 3:1 with total flow of 75 ml min^{-1}, 0.5 g SSZ-13 (or SAPO-34), total pressure 200 psig with partial pressure of CH_3OH ~6 psig.

less. Yet, the cumulative P/O in the presence of H_2 was found to increase, indicating that secondary hydrogenation of olefins occurred over the BAS of SSZ-13 and SAPO-34. Further, the cumulative P/O ratio was higher over SSZ-13 (~13 at 1474 mol$_C$/mol$_{H+}$ in Fig. 6C), compared to SAPO-34 (0.6 at 1041 mol$_C$/mol$_{H+}$ in Fig. 6F), which can be attributed to higher secondary hydrogenation of olefins over the BAS of SSZ-13 in line with its higher BAS strength.

We further assessed the influence of the partial pressure of H_2 (p_{H_2}) on the cumulative C_3/C_2 and cumulative P/O ratios, as illustrated in Fig. 7 at an *iso*-cumulative TON of ~1100 mol$_C$/mol$_{H+}$. As depicted in Fig. 7, increasing p_{H_2} from 0 to 340 psig enhanced the cumulative C_3/C_2 ratio by ~13 × over SSZ-13 (1.2 to 16), however, only by ~1.2 × over SAPO-34 (2.6 to 3). Similarly, the cumulative P/O ratio (shown in Fig. 7B) increased ~35 × (0.6 to 21) over SSZ-13 with increasing p_{H_2} from 0 to 340 psig, while the cumulative P/O increased ~3 × (0.07 to 0.2) over SAPO-34. Taken together, we infer that the olefin cycle propagated more and led to more secondary hydrogenation of olefins with increasing p_{H_2} over the higher BAS strength of SSZ-13.

Combining the findings above, as shown in Fig. 8A, we propose that during the tandem CO_2 hydrogenation over interpellet_In_2O_3/SSZ-13, the propagation of the olefin cycle was favored in the presence of H_2. However, the formation of paraffins did not happen solely *via* the HT, as the propagation of the aromatic cycle was hindered. Rather, paraffins were formed *via* the secondary hydrogenation of olefins over the BAS of SSZ-13 (see Fig. 8A). We posit that the secondary hydrogenation of olefins (P/O ~21 at TON ~1100 mol$_C$/mol$_{H+}$) consumed the olefins that seed the aromatic cycle in SSZ-13. Similarly, in the case of interpellet_In_2O_3/SAPO-34, the propagation of the olefin cycle was favored in the presence of H_2; however, the paraffins formed *via* secondary hydrogenation (cumulative P/O ~0.2) over the BAS of SAPO-34 were much less compared to SSZ-13 due to its lower acid strength [36,38], as indicated by a lower cumulative C_3/C_2 ratio of ~3 (see Fig. 8B). Nonetheless, in both cases, secondary hydrogenation of olefins in the presence of H_2 likely suppressed the formation of aromatics and gave better stability of SSZ-13 and SAPO-34. This was further confirmed by the occluded HC analysis. The identification of the aromatics formed over spent interpellet_In_2O_3/SSZ-13 and interpellet_In_2O_3/SAPO-34 is shown in Fig. 9A and B. The product distribution of aromatics in Fig. 9C shows both interpellet_In_2O_3/SSZ-13 and interpellet_In_2O_3/SAPO-34 formed lesser polycyclic aromatics during tandem CO_2 hydrogenation (~35 % and ~46 % of total anthracenes and pyrenes formed over interpellet_In_2O_3/SSZ-13 and interpellet_In_2O_3/SAPO-34, respectively), compared to MTO (81 % and 83 % of total anthracenes and pyrenes formed over SSZ-13 and SAPO-34, respectively as shown in Fig. 3C). This is further evident from ^{13}C SSNMR spectra of spent interpellet_In_2O_3/SSZ-13 and interpellet_In_2O_3/SAPO-34 (see Fig. 9D) where the ratio of peak areas for aromatics to alkyl groups was lower over spent interpellet_In_2O_3/SSZ-13 and interpellet_In_2O_3/SAPO-34 ($A_{aromatic}/A_{alkyl}$ ratio 0.8 and 0.6, respectively), as compared to SSZ-13 and SAPO-34 during MTO ($A_{aromatic}/A_{alkyl}$ ratio 4.9 and 2.1 over SSZ-13 and SAPO-34, respectively, as shown in Fig. 3D). Therefore, we conclude that the secondary hydrogenation of olefins in the presence of H_2 suppressed the formation of polycyclic aromatics and provided stability of SSZ-13 and SAPO-34 during tandem CO_2 hydrogenation.

Additionally, we performed MTO with CO_2 co-feed over SSZ-13 and observed minimal changes in CH_3OH conversion and HC distribution (see Fig. S5), as compared to MTO over SSZ-13 (Fig. 2A and B), indicating that CO_2 likely does not influence the relative propagation of

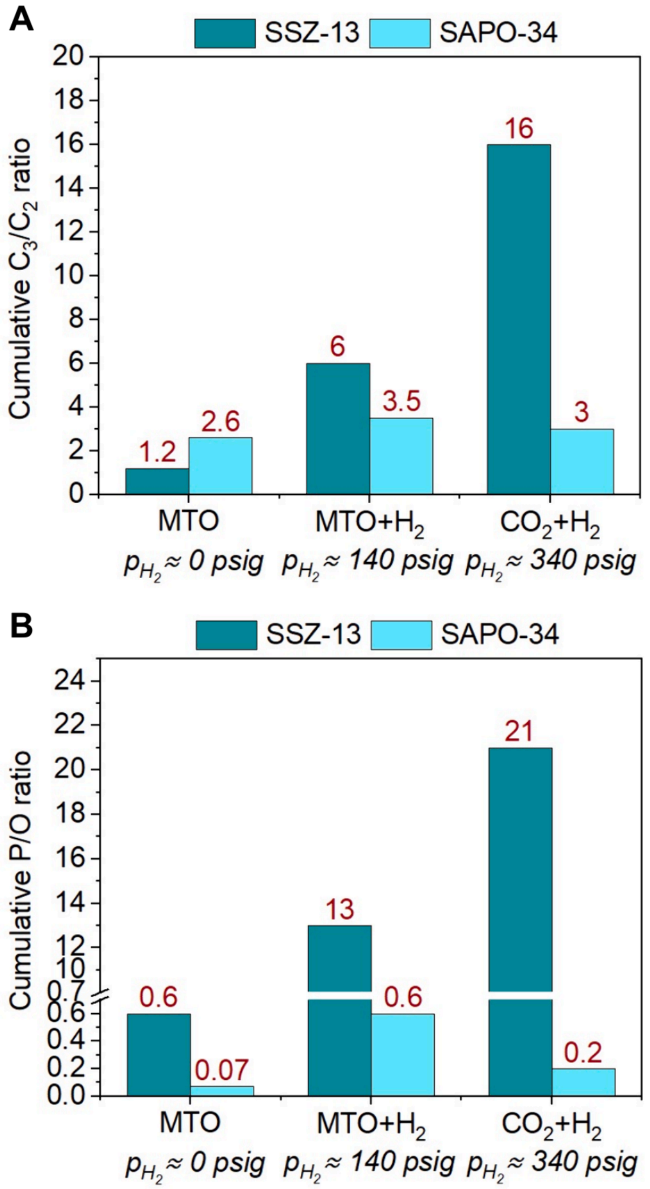

Fig. 7. Influence of the partial pressure of H_2 (p_{H_2}) on (A) cumulative C_3 (propane and propylene)-to-C_2 (ethane and ethylene) ratio and (B) cumulative paraffin-to-olefin (P/O), at cumulative turnover number (TON) of ~1100 mol_C/mol_{H+}.

olefin and aromatic cycles. Nonetheless, we note that the partial pressure of CO and CH_3OH could influence the relative propagation of olefin and aromatic cycles during tandem CO_2 hydrogenation. Bhan and co-workers reported that the presence of CO and CH_3OH could favor the propagation of the aromatic cycle *via* carbonylation and Prins condensation during MTO, respectively [40–42]. In fact, for MTO at a higher CH_3OH partial pressure of ~14 psi (see Fig. S4) compared to ~6 psi in Fig. 1, both SSZ-13 and SAPO-34 deactivated faster, showed higher cumulative P/O and lower cumulative C_3/C_2, consistent with propagation of the aromatic cycle.

However, during tandem CO_2 hydrogenation, the partial pressure of CH_3OH (p_{CH_3OH} ~1 psi) and CO (p_{CO} ~30 psi) were found to be at least one order of magnitude lower than the partial pressure of H_2 (~340 psig) (see Table S2). As such, their effects on HCP were likely not dominant, which is further evident from the preferential olefin cycle propagation over the aromatic cycle with increasing p_{H_2} over both SSZ-13 and SAPO-34 (Fig. 8A). This observation is further consistent with previous studies where no change in aromatic and olefin cycles was observed for $p_{CO} < 45$ psi [41,65,66].

3.2.2. *Intrapellet admixture of In_2O_3/SSZ-13 and In_2O_3/SAPO-34*

Bifunctional oxide-zeolite catalysts often exhibit proximity-dependent reactivity during tandem CO_2 hydrogenation [7,9,15,24,67]. Therefore, we further evaluated the performance of SSZ-13 and SAPO-34 in combination with In_2O_3 in intrapellet admixtures with nanoscale proximity between redox and acid sites (prepared *via* mixing In_2O_3 with SSZ-13 and SAPO-34 powders in an agate mortar, respectively), denoted as intrapellet_In_2O_3/SSZ-13 and intrapellet_In_2O_3/SAPO-34, respectively. Interestingly, intrapellet_In_2O_3/SSZ-13 and intrapellet_In_2O_3/SAPO-34 formed predominantly CH_4 (92 % and 75 % in HC distribution, respectively) at a similar CO_2 conversion of 21 %, as shown in Fig. 10A, B. The reduced reactivity in intrapellet admixtures might occur due to (i) structural damage of the microporous structure of the zeolite/zeotype [68], and/or (ii) ion exchange of proton sites of the zeolite/zeotype with cationic species from the metal oxide, which may alter their acidic properties [6,69–72].

3.2.2.1. *Structural, textural, and morphological properties of intrapellet admixtures.*

To assess the morphological structure of intrapellet_In_2O_3/SSZ-13 and intrapellet_In_2O_3/SAPO-34, transmission electron micrographs (TEM) were obtained, as shown in Fig. S14A and B. These depict In_2O_3 particles (~10 nm, circled in yellow) distributed on the surface of SSZ-13 (~900 nm) and SAPO-34 (~2000 nm) with comparable size and shape of pristine SSZ-13 (~1000 nm) and SAPO-34 (~2000 nm), respectively (see Fig. S12A, B). Further, powder X-ray diffraction (PXRD) patterns of intrapellet_In_2O_3/SSZ-13 and intrapellet_In_2O_3/SAPO-34 in Fig. S18 showed that the crystallinity of SSZ-13 (with peaks at 9.8°, 20.9°, and 31.1° in Fig. S12D) and SAPO-34 (with an intense peak at 9.8° and weak peaks at 20.8° and 31.0° in Fig. S12D) were retained in intrapellet admixtures [73,74]. Argon physisorption analysis further revealed that the micropore volume of SSZ-13 and SAPO-34 in intrapellet_In_2O_3/SSZ-13 (0.08 cc/g) and intrapellet_In_2O_3/SAPO-34 (0.05 cc/g) were mostly retained (see Table S4). Taken together, our data suggests that the drastic shift of HC distribution to CH_4 exhibited by intrapellet_In_2O_3/SSZ-13 and intrapellet_In_2O_3/SAPO-34 was not caused by any structural damage to SSZ-13 and SAPO-34 during their preparation.

3.2.2.2. *Ion exchange of BAS (H^+) with $In^{\delta+}$ in intrapellet admixtures.*

To probe whether the inhibited catalytic activity of intrapellet_In_2O_3/SSZ-13 and intrapellet_In_2O_3/SAPO-34 was caused by ion-exchange of BAS with cationic species from In_2O_3, we deliberately exchanged BAS of SSZ-13 and SAPO-34 with $In^{\delta+}$ (δ likely to be 3) ions with In:Al ratio 3.5 and In:Si ratio 1, respectively, denoted as In-SSZ-13 and In-SAPO-34 and evaluated their catalytic activity as an interpellet admixture with In_2O_3 to avoid any structural change that may occur in the preparation of intrapellet admixtures (denoted as interpellet_In_2O_3/In-SSZ-13 and interpellet_In_2O_3/In-SAPO-34, respectively). Interestingly, as shown in Fig. 10A,B, both interpellet_In_2O_3/In-SSZ-13 and interpellet_In_2O_3/In-SAPO-34 formed more CH_4 (53 % and 97 % in HC distribution, respectively), compared to interpellet_In_2O_3/SSZ-13 and interpellet_In_2O_3/SAPO-34 (3.5 and 32.9 % in HC distribution, respectively). Therefore, we posit that the formation of CH_4 over intrapellet_In_2O_3/SSZ-13 and intrapellet_In_2O_3/SAPO-34 was likely caused by the ion-exchange between H^+ and $In^{\delta+}$ [6,69–72]. It is to be noted that the space–time yield (STY) of C_{2+} HC was higher over interpellet_In_2O_3/In-SSZ-13 (2.6×10^{-5} mol_C g_{cat}^{-1} min^{-1}, see Fig. S19A), as compared to interpellet_In_2O_3/In-SAPO-34 (4.3×10^{-7} mol_C g_{cat}^{-1} min^{-1}, see Fig. S19B), likely due to having more BAS remaining after ion exchange *via* IWI (BAS density 0.58 mmol/g and 0.31 mmol/g in In-SSZ-13 and In-SAPO-34, respectively, as shown in Fig. S19C and D). Therefore, although $In^{\delta+}$ loading was higher in In-SSZ-13 (In:Al ratio 3.5), as

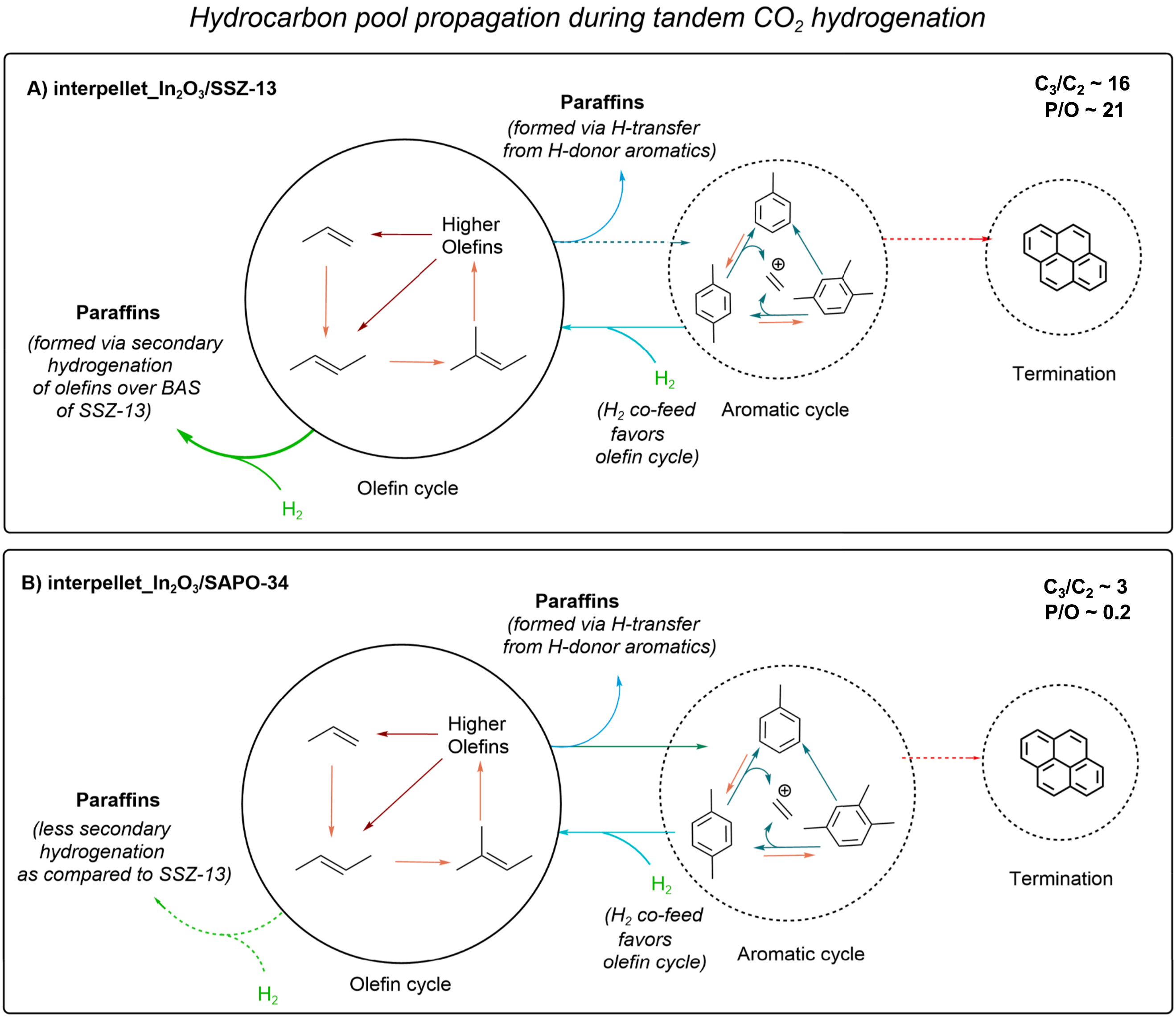

Fig. 8. Influence of acid strength on hydrocarbon pool (HCP) mechanism during tandem hydrogenation of CO_2 over (A) interpellet_In_2O_3/SSZ-13 and (B) interpellet_In_2O_3/SAPO-34 at cumulative turnover number (TON) ~1100 mol_C/mol_{H+}. For simplification, CH_3OH synthesis over In_2O_3 was not shown in the scheme.

compared to In-SAPO-34 (In:Si ratio 1), ion exchange was ~2 × lesser for In-SSZ-13. This observation is consistent with the TEM micrograph of In-SSZ-13 where the number of In_2O_3 particles was higher on the surface of SSZ-13 as compared to SAPO-34 (shown in Fig. S18C and D, respectively). Nonetheless, regardless of the extent of ion exchange, both interpellet_In_2O_3/In-SSZ-13 and interpellet_In_2O_3/In-SAPO-34 exhibited lower C_{2+} selectivity and higher CH_4 selectivity, as compared to interpellet_In_2O_3/SSZ-13 and interpellet_In_2O_3/SAPO-34, respectively (see Fig. 10A, B), because of ion exchange of BAS with $In^{\delta+}$.

We further compared the catalytic performance of intrapellet_In_2O_3/SSZ-13 and intrapellet_In_2O_3/SAPO-34 with interpellet admixtures of In_2O_3 with non-acidic Na-SSZ-13 and Na-SAPO-34 (Na^+ ion exchanged SSZ-13 and SAPO-34) in Fig. S17. As expected, both interpellet_In_2O_3/Na-SSZ-13 and interpellet_In_2O_3/Na-SAPO-34 formed predominantly CH_4 (as shown in Fig. S17C and D), similar to intrapellet_In_2O_3/SSZ-13 and intrapellet_In_2O_3/SAPO-34, confirming that the exchange of BAS with $In^{\delta+}$ inhibited C–C coupling. We further performed Fourier transform infrared (FTIR) spectroscopy of pristine intrapellet_In_2O_3/SSZ-13 (see Fig. S16), where the band corresponding to BAS of SSZ-13 at wavenumbers of 3598 cm^{-1} was found to be greatly reduced, *akin* to pristine In-SSZ-13. Interestingly, the BAS peak of intrapellet_In_2O_3/SSZ-13 was found to be completely reduced in the presence of H_2 at a temperature of 350 °C (reaction temperature), as shown in Fig. S16.

Although we observed In_2O_3 particles on the surface of SSZ-13 and SAPO-34 in intrapellet_In_2O_3/SSZ-13 (Fig. S14A) and intrapellet_In_2O_3/SAPO-34 (Fig. S14B) in TEM, we could not definitively probe the ion exchange between BAS and $In^{\delta+}$ in these admixtures. Hence, we conducted X-ray photoelectron spectroscopy (XPS) on intrapellet_In_2O_3/SSZ-13, intrapellet_In_2O_3/SAPO-34, In-SSZ-13, and In-SAPO-34, and compared them with bulk In_2O_3, as shown in Fig. 10C and D. Bulk In_2O_3 exhibited characteristic peaks at binding energy (B.E.) values of 443.9 and 451.4 eV for $In3d_{5/2}$ and $In3d_{3/2}$ in Fig. 10C and D, respectively, which is consistent with previous reports [72,75,76]. Pristine intrapellet_In_2O_3/SSZ-13 and In-SSZ-13 exhibited peaks at 443.9 and 451.4 eV similar to bulk In_2O_3. This was expected as intrapellet_In_2O_3/SSZ-13 and In-SSZ-13 had In:Al ratio of 4.5 and 3.5, respectively, indicating an excess amount of In compared to the amount of BAS available for ion exchange. This is consistent with the TEM of intrapellet_In_2O_3/SSZ-13 and In-SSZ-13 in Figs. S14A and S18C, respectively, where In_2O_3 particles were visible on the SSZ-13 surface. Interestingly, XPS for both

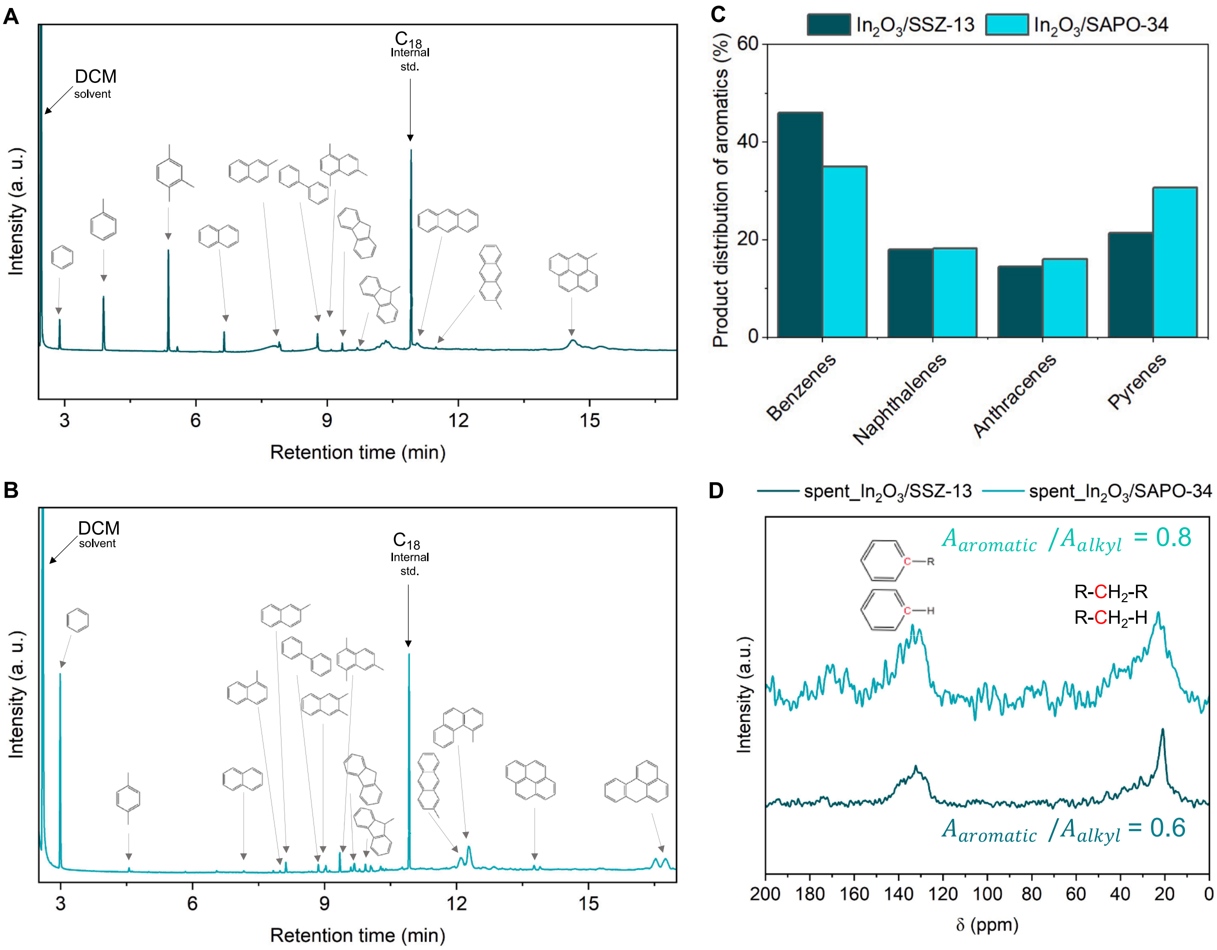

Fig. 9. Occluded hydrocarbon (HC) formed over SSZ-13 and SAPO-34 in intrapellet admixtures during tandem CO_2 hydrogenation. (A) Chromatogram by gas chromatograph and mass spectrometer (GCMS) identifying the aromatics formed over spent interpellet_In_2O_3/SSZ-13. (B) Chromatogram by GCMS identifying the aromatics formed over spent interpellet_In_2O_3/SAPO-34. (C) Aromatic distribution of coke species formed over interpellet_In_2O_3/SSZ-13 and interpellet_In_2O_3/SAPO-34. (D) Solid-state ^{13}C nuclear magnetic resonance (NMR) spectra conducted over spent interpellet_In_2O_3/SSZ-13 and interpellet_In_2O_3/SAPO-34.

samples exhibited additional lower B.E. peaks at 440.7 and 448.3 eV (see Fig. 10C). Previously, Gabrienko *et al.* observed similar lower B.E. peaks for In ion-exchanged HZSM-5 (Si:Al ratio 17), likely due to the formation of In^+ [72]. Therefore, the peaks at 440.7 and 448.3 eV could likely be related to ion-exchanged $In^{\delta+}$ species at a lower oxidation state ($\delta < 3$) in general, and In^+ in particular [69–72,77,78]. Additionally, the ratio of the peak area of In_2O_3 and $In^{\delta+}$ species (denoted as $A_{In^{3+}}/A_{In^{\delta+}}$ in Fig. 10C) was found to be higher for intrapellet_In_2O_3/SSZ-13 (3) than In-SSZ-13 (0.9), indicating that the amount of bulk In_2O_3 present in intrapellet_In_2O_3/SSZ-13 was higher than In-SSZ-13. This is consistent with the higher In:Al ratio in intrapellet_In_2O_3/SSZ-13 (4.5), as compared to In-SSZ-13 (3.5).

Similarly, in the case of intrapellet_In_2O_3/SAPO-34 and In-SAPO-34, peaks at 443.9 and 451.4 eV corresponding to bulk In_2O_3 were observed (see Fig. 10D). Interestingly, intrapellet_In_2O_3/SAPO-34 and In-SAPO-34 exhibited additional peaks at higher B.E. for $In3d_{3/2}$ and $In3d_{5/2}$ at 444 and 452 eV, as compared to In_2O_3, likely indicating a stronger interaction of $In^{\delta+}$ species (δ likely to be 3) with SAPO-34 [6,68,72]. Again, considering the ratio of $A_{In^{3+}}/A_{In^{\delta+}}$ in Fig. 10D, the value was higher for intrapellet_In_2O_3/SAPO-34 (7), as compared to In-SAPO-34 (0.5), indicating that intrapellet_In_2O_3/SAPO-34 contained more In_2O_3 than In-SAPO-34. This was expected as the In:Si ratio was ~5 × higher in intrapellet_In_2O_3/SAPO-34 (5) than In-SAPO-34 (1), thereby having more In present than the amount of BAS.

Regarding the higher B.E. peaks observed in intrapellet_In_2O_3/SAPO-34 and In-SAPO-34 in Fig. 10D, a similar observation was previously reported for intrapellet admixture of In_2O_3 and HZSM-5 (Si:Al ratio 40), where higher B.E peaks at 445.6 and 453.2 eV were exhibited by ion-exchanged $In^{\delta+}$ species [57,78]. Mihályi *et al.* attributed these higher B.E. peaks to InO^+ species (reported for HZSM-5, Si:Al ratio 30) [79–81]. The study further reported that the oxidation state of $In^{\delta+}$ ($InO^+ \leftrightarrow In^+$) could be reversible where InO^+ could reduce and convert to In^+ ($InO^+Z^- + H_2 \rightarrow In^+Z^- + H_2O$; Z denotes zeolite framework) under reductive conditions (10)% H_2, 500 °C, 1 h) [72,81]. More importantly, they observed the oxidation state of $In^{\delta+}$ species could be affected by the acidity of the zeolite, as HZSM-5 (Si:Al ratio 30) formed more oxidized $In^{\delta+}$ species than Y (Si:Al ratio 2.5) [81]. Based on these observations, we posit that the difference in the oxidation state of ion-exchanged $In^{\delta+}$ species in SSZ-13 and SAPO-34 could be attributed to the difference in their acid strengths where the higher BAS strength of SSZ-13 could form In^+ [79,80], while weaker acid strength of SAPO-34 could form InO^+ [79–81]. However, our data demonstrated that regardless of the different acid strengths of SSZ-13 and SAPO-34, the ion exchange of BAS with $In^{\delta+}$ altered their acidic properties in their intrapellet admixtures with In_2O_3 (as shown in Figs. S16 and S17).

4. Conclusion

In this study, we revealed that unlike methanol-to-olefins (MTO), where SSZ-13 and SAPO-34 deactivated *via* coking, deactivation during tandem hydrogenation of CO_2 over an interpellet admixture of In_2O_3 with SSZ-13 and SAPO-34 could be circumvented in the presence of H_2.

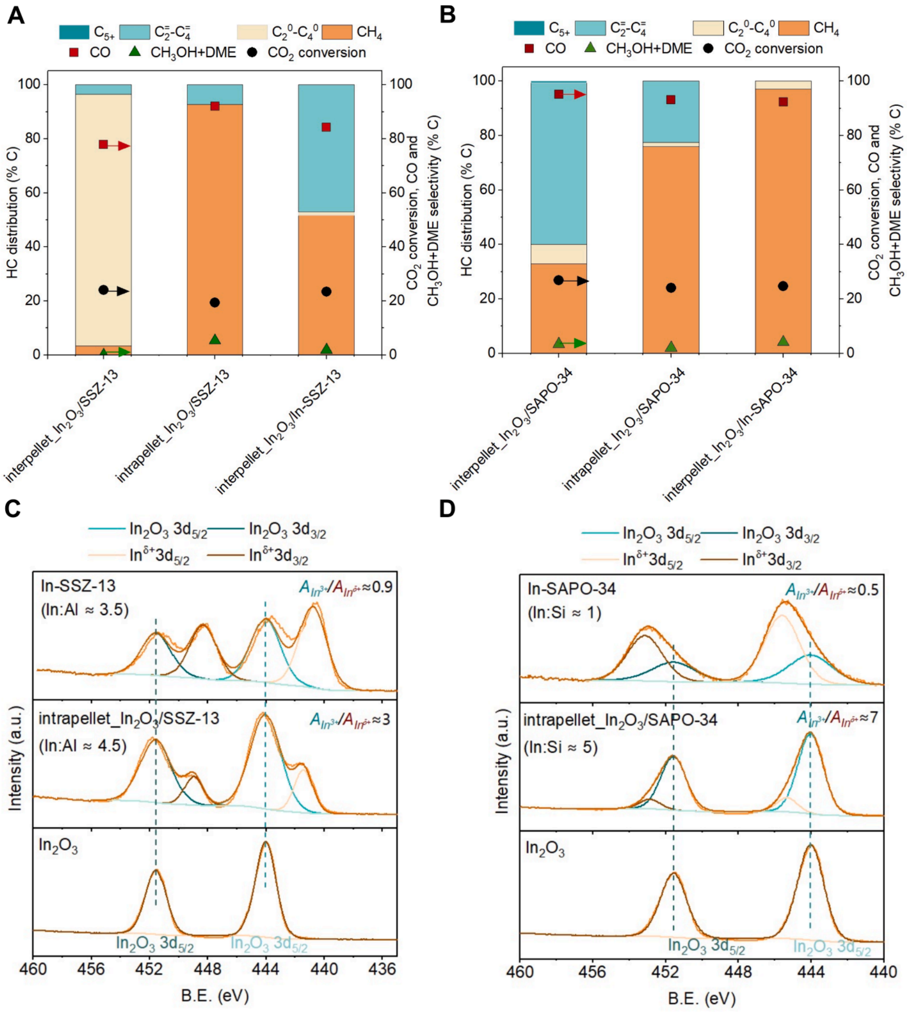

Fig. 10. Probing ion exchange of H^+ with $In^{\delta+}$ in intrapellet admixtures. (A) Catalytic performance of interpellet_In_2O_3/SSZ-13, intrapellet_In_2O_3/SSZ-13 and interpellet_In_2O_3/In-SSZ-13 during CO_2 hydrogenation. The left axis shows HC distribution, and the right axis shows CO_2 conversion, CO, and CH_3OH + DME selectivity. Reaction conditions: 350 °C, 500 psig, 9000 ml $g_{cat}^{-1}h^{-1}$, H_2:CO_2 ratio 3:1, In_2O_3:SSZ-13 mass ratio 1:1. (B) Catalytic performance of interpellet_In_2O_3/SAPO-34, intrapellet_In_2O_3/SAPO-34 and interpellet_In_2O_3/In-SAPO-34 during CO_2 hydrogenation. Reaction conditions: 350 °C, 500 psig, 9000 ml $g_{cat}^{-1}h^{-1}$, H_2:CO_2 ratio 3:1, In_2O_3:SAPO-34 mass ratio 1:1. (C) X-ray photoelectron spectroscopy (XPS) of In_2O_3, intrapellet_In_2O_3/SSZ-13 and In-SSZ-13. (D) XPS of In_2O_3, intrapellet_In_2O_3/SAPO-34 and In-SAPO-34.

The presence of H_2 favored the olefin cycle propagation over the aromatic cycle, and caused secondary hydrogenation of olefins to paraffins, thereby suppressing olefin aromatization and the formation of deactivation-inducing polycyclic aromatics. Additionally, interpellet_In_2O_3/SSZ-13 predominantly formed paraffins (93 % in the HC distribution, and paraffin-to-olefin ratio, P/O ~21) over SSZ-13 with its higher BAS strength, while interpellet_In_2O_3/SAPO-34 formed olefins (67 % in the HC distribution) due to less secondary hydrogenation (P/O ~0.2) over SAPO-34 with its lower BAS strength. The data further revealed that the catalytic performance of SSZ-13 and SAPO-34 during CO_2 hydrogenation was inhibited as the redox sites of In_2O_3 and BAS of SSZ-13 and SAPO-34 were integrated at nanoscale proximity as intrapellet admixtures, due to ion-exchange of BAS with cationic species ($In^{\delta+}$) from In_2O_3, eventually leading to the formation of CH_4 (92 % and 75 % in HC distribution over intrapellet_In_2O_3/SSZ-13 and intrapellet_In_2O_3/SAPO-34, respectively). Overall, this study provides mechanistic insights and underpinnings into the critical role played by the BAS strength in controlling HC product selectivity and catalyst stability during tandem CO_2 hydrogenation.

CRediT authorship contribution statement

Fatima Mahnaz: Conceptualization, Writing – original draft, Writing – review & editing, Investigation, Formal analysis, Data curation. **Jasan Robey Mangalindan:** Writing – review & editing, Data curation, Investigation. **Jenna Vito:** Writing – review & editing, Data curation, Investigation. **Ryan Helmer:** Writing – review & editing, Data curation, Investigation. **Manish Shetty:** Conceptualization, Writing – review & editing, Supervision, Funding acquisition.

Declaration of competing interest

The authors declare that they have no known competing financial interests or personal relationships that could have appeared to influence the work reported in this paper.

Data availability

Data will be made available on request.

Acknowledgments

We are grateful to the Artie McFerrin Department of Chemical Engineering at Texas A&M University, the College of Engineering, Dr. Mark Barteau, and the Provost for their financial support. This work was funded by Texas A&M University (TAMU), Texas A&M Engineering Experiment Station (TEES), the Governor's University Research Initiative (GURI), the Oak Ridge Associated Universities through their Ralph E. Powe Junior Faculty Enhancement Award, and the National Science Foundation (NSF) CBET grant number 2245474. MS acknowledges partial support from Texas A&M University System's National Laboratory Office (NLO) for their Development Fellowship. We thank Yu-Ting Lu and Prof. Mustafa Akbulut for their assistance with collecting transmission electron microscopy (TEM). We also acknowledge that the XPS characterization of the catalyst powders was performed in the Texas A&M University Materials Characterization Core Facility (RRID: SCR_022202), TEM characterization was performed at Texas A&M University Microscopy and Imaging Center (MIC) (RRID:SCR_022128).

Appendix A. Supplementary material

Supplementary data to this article can be found online at https://doi.org/10.1016/j.jcat.2024.115518.

References

[1] P. Gao, S. Li, X. Bu, S. Dang, Z. Liu, H. Wang, L. Zhong, M. Qiu, C. Yang, J. Cai, Direct conversion of CO2 into liquid fuels with high selectivity over a bifunctional catalyst, Nat. Chem. 9 (2017) 1019–1024.

[2] P. Gao, S. Dang, S. Li, X. Bu, Z. Liu, M. Qiu, C. Yang, H. Wang, L. Zhong, Y. Han, Direct production of lower olefins from CO2 conversion via bifunctional catalysis, ACS Catal. 8 (2018) 571–578.

[3] Y. Wang, L. Tan, M. Tan, P. Zhang, Y. Fang, Y. Yoneyama, G. Yang, N. Tsubaki, Rationally designing bifunctional catalysts as an efficient strategy to boost CO2 hydrogenation producing value-added aromatics, ACS Catal. 9 (2018) 895–901.

[4] D. Wang, Z. Xie, M.D. Porosoff, J.G. Chen, Recent advances in carbon dioxide hydrogenation to produce olefins and aromatics, Chem 7 (2021) 2277–2311.

[5] Y. Wang, X. Gao, M. Wu, N. Tsubaki, Thermocatalytic hydrogenation of CO2 into aromatics by tailor-made catalysts: recent advancements and perspectives, EcoMat 3 (2021) e12080.

[6] Y. Wang, G. Wang, L.I. van der Wal, K. Cheng, Q. Zhang, K.P. de Jong, Y. Wang, Visualizing element migration over bifunctional metal-zeolite catalysts and its impact on catalysis, Angew. Chem. 133 (2021) 17876–17884.

[7] F. Mahnaz, V. Dunlap, R. Helmer, S.S. Borkar, R. Navar, X. Yang, M. Shetty, Selective valorization of CO2 towards valuable hydrocarbons through methanol-mediated tandem catalysis, ChemCatChem 15 (2023) e202300402.

[8] P. Sharma, J. Sebastian, S. Ghosh, D. Creaser, L. Olsson, Recent advances in hydrogenation of CO 2 into hydrocarbons via methanol intermediate over heterogeneous catalysts, Catalysis, Sci. Technol. 11 (2021) 1665–1697.

[9] Y. Gambo, S. Adamu, R.A. Lucky, M.S. Ba-Shammakh, M.M. Hossain, Tandem catalysis: a sustainable alternative for direct hydrogenation of CO2 to light olefins, Appl. Catal. A 641 (2022) 118658.

[10] L. Samiee, S. Gandzha, Power to methanol technologies via CO2 recovery: CO2 hydrogenation and electrocatalytic routes, Rev. Chem. Eng. 37 (2021) 619–641.

[11] Z. He, M. Cui, Q. Qian, J. Zhang, H. Liu, B. Han, Synthesis of liquid fuel via direct hydrogenation of CO2, Proc. Natl. Acad. Sci. 116 (2019) 12654–12659.

[12] J. Xie, U. Olsbye, The oxygenate-mediated conversion of COx to hydrocarbons— on the role of zeolites in tandem catalysis, Chem. Rev. (2023).

[13] A. Livescu, R. Navar, J.R. Mangalindan, F. Mahnaz, Y. Ge, M. Shetty, X. Yang, Catalysts for Clean Energy: A Review on Current Progress for the Catalyzed Recycling of CO2 into Dimethyl Ether, Topics in Catalysis (2024) 1–22.

[14] Z. Li, Y. Qu, J. Wang, H. Liu, M. Li, S. Miao, C. Li, Highly selective conversion of carbon dioxide to aromatics over tandem catalysts, Joule 3 (2019) 570–583.

[15] J. Mou, X. Fan, F. Liu, X. Wang, T. Zhao, P. Chen, Z. Li, C. Yang, J. Cao, CO2 hydrogenation to lower olefins over Mn2O3-ZnO/SAPO-34 tandem catalysts, Chem. Eng. J. 421 (2021) 129978.

[16] S. Dang, P. Gao, Z. Liu, X. Chen, C. Yang, H. Wang, L. Zhong, S. Li, Y. Sun, Role of zirconium in direct CO2 hydrogenation to lower olefins on oxide/zeolite bifunctional catalysts, J. Catal. 364 (2018) 382–393.

[17] J. Li, T. Yu, D. Miao, X. Pan, X. Bao, Carbon dioxide hydrogenation to light olefins over ZnO-Y2O3 and SAPO-34 bifunctional catalysts, Catal. Commun. 129 (2019) 105711.

[18] S. Lu, H. Yang, Z. Zhou, L. Zhong, S. Li, P. Gao, Y. Sun, Effect of In2O3 particle size on CO2 hydrogenation to lower olefins over bifunctional catalysts, Chin. J. Catal. 42 (2021) 2038–2048.

[19] F. Meng, P. Zhang, L. Ma, G. Yang, R. Zhang, B. Wang, Y. Hu, Z. Li, Unraveling the role of GaZrOx structure and oxygen vacancy in bifunctional catalyst for highly active and selective conversion of syngas into light olefins, Chem. Eng. J. 467 (2023) 143500.

[20] S. Teketel, M.W. Erichsen, F.L. Bleken, S. Svelle, K.P. Lillerud, U. Olsbye, Shape selectivity in zeolite catalysis. The Methanol to Hydrocarbons (MTH) reaction, Catalysis 26 (2014) 179–217.

[21] U. Olsbye, S. Svelle, M. Bjørgen, P. Beato, T.V. Janssens, F. Joensen, S. Bordiga, K. P. Lillerud, Conversion of methanol to hydrocarbons: how zeolite cavity and pore size controls product selectivity, Angew. Chem. Int. Ed. 51 (2012) 5810–5831.

[22] Y. Bhawe, M. Moliner-Marin, J.D. Lunn, Y. Liu, A. Malek, M. Davis, Effect of cage size on the selective conversion of methanol to light olefins, ACS Catal. 2 (2012) 2490–2495.

[23] S. Tada, H. Kinoshita, N. Ochiai, A. Chokkalingam, P. Hu, N. Yamauchi, Y. Kobayashi, K. Iyoki, Search for solid acid catalysts aiming at the development of bifunctional tandem catalysts for the one-pass synthesis of lower olefins via CO2 hydrogenation, Int. J. Hydrogen Energy 46 (2021) 36721–36730.

[24] Y. Li, M. Wang, S. Liu, F. Wu, Q. Zhang, S. Zhang, K. Cheng, Y. Wang, Distance for communication between metal and acid sites for syngas conversion, ACS Catal. 12 (2022) 8793–8801.

[25] S. Ilias, A. Bhan, Mechanism of the catalytic conversion of methanol to hydrocarbons, ACS Catal. 3 (2013) 18–31.

[26] S. Ilias, A. Bhan, Tuning the selectivity of methanol-to-hydrocarbons conversion on H-ZSM-5 by co-processing olefin or aromatic compounds, J. Catal. 290 (2012) 186–192.

[27] C.-M. Wang, Y.-D. Wang, Z.-K. Xie, Insights into the reaction mechanism of methanol-to-olefins conversion in HSAPO-34 from first principles: are olefins themselves the dominating hydrocarbon pool species? J. Catal. 301 (2013) 8–19.

[28] L. Yang, C. Wang, W. Dai, G. Wu, N. Guan, L. Li, Progressive steps and catalytic cycles in methanol-to-hydrocarbons reaction over acidic zeolites, Fund. Res. 2 (2022) 184–192.

[29] C.-M. Wang, Y.-D. Wang, Z.-K. Xie, Verification of the dual cycle mechanism for methanol-to-olefin conversion in HSAPO-34: a methylbenzene-based cycle from DFT calculations, Catal. Sci. Technol. 4 (2014) 2631–2638.

[30] A.D. Chowdhury, A.L. Paioni, K. Houben, G.T. Whiting, M. Baldus, B. M. Weckhuysen, Bridging the gap between the direct and hydrocarbon pool mechanisms of the methanol-to-hydrocarbons process, Angew. Chem. Int. Ed. 57 (2018) 8095–8099.

[31] I.M. Hill, S. Al Hashimi, A. Bhan, Kinetics and mechanism of olefin methylation reactions on zeolites, J. Catal. 285 (2012) 115–123.

[32] S. Ilias, A. Bhan, The mechanism of aromatic dealkylation in methanol-to-hydrocarbons conversion on H-ZSM-5: what are the aromatic precursors to light olefins? J. Catal. 311 (2014) 6–16.

[33] A. Hwang, A. Bhan, Deactivation of zeolites and zeotypes in methanol-to-hydrocarbons catalysis: mechanisms and circumvention, Acc. Chem. Res. 52 (2019) 2647–2656.

[34] M. Bjørgen, S. Svelle, F. Joensen, J. Nerlov, S. Kolboe, F. Bonino, L. Palumbo, S. Bordiga, U. Olsbye, Conversion of methanol to hydrocarbons over zeolite H-ZSM-5: On the origin of the olefinic species, J. Catal. 249 (2007) 195–207.

[35] S. Müller, Y. Liu, F.M. Kirchberger, M. Tonigold, M. Sanchez-Sanchez, J.A. Lercher, Hydrogen transfer pathways during zeolite catalyzed methanol conversion to hydrocarbons, J. Am. Chem. Soc. 138 (2016) 15994–16003.

[36] S.S. Arora, Z. Shi, A. Bhan, Mechanistic basis for effects of high-pressure H2 cofeeds on methanol-to-hydrocarbons catalysis over zeolites, ACS Catal. 9 (2019) 6407–6414.

[37] Z. Shi, A. Bhan, Metrics of performance relevant in methanol-to-hydrocarbons catalysis, J. Catal. 421 (2023) 198–209.

[38] Z. Shi, M. Neurock, A. Bhan, Methanol-to-olefins catalysis on HSSZ-13 and HSAPO-34 and its relationship to acid strength, ACS Catal. 11 (2021) 1222–1232.

[39] S. Xing, S. Turner, D. Fu, S. van Vreeswijk, Y. Liu, J. Xiao, R. Oord, J. Sann, B. M. Weckhuysen, Silicalite-1 layer secures the bifunctional nature of a CO2 hydrogenation catalyst, JACS Au 3 (2023) 1029–1038.

[40] Z. Shi, A. Bhan, Methanol-to-olefins catalysis on window-cage type zeolites/zeotypes with syngas co-feeds: understanding syngas-to-olefins chemistry, J. Catal. 413 (2022) 913–922.

[41] Z. Shi, A. Bhan, The effects of CO co-feed on the catalytic performance of Methanol-to-Hydrocarbons conversion on HZSM-5, Chem. Eng. J. 456 (2023) 140867.

[42] S.S. Arora, A. Bhan, The critical role of methanol pressure in controlling its transfer dehydrogenation and the corresponding effect on propylene-to-ethylene ratio during methanol-to-hydrocarbons catalysis on H-ZSM-5, J. Catal. 356 (2017) 300–306.

[43] Z. Li, J. Wang, Y. Qu, H. Liu, C. Tang, S. Miao, Z. Feng, H. An, C. Li, Highly selective conversion of carbon dioxide to lower olefins, ACS Catal. 7 (2017) 8544–8548.

[44] L. Tan, P. Zhang, Y. Cui, Y. Suzuki, H. Li, L. Guo, G. Yang, N. Tsubaki, Direct CO2 hydrogenation to light olefins by suppressing CO by-product formation, Fuel Process. Technol. 196 (2019) 106174.

[45] J. Gao, C. Jia, B. Liu, Direct and selective hydrogenation of CO 2 to ethylene and propene by bifunctional catalysts, Catal. Sci. Technol. 7 (2017) 5602–5607.

[46] M. Ghasemi, M. Mohammadi, M. Sedighi, Sustainable production of light olefins from greenhouse gas CO2 over SAPO-34 supported modified cerium oxide, Micropor. Mesopor. Mater. 297 (2020) 110029.

[47] Z. Liu, Y. Ni, T. Sun, W. Zhu, Z. Liu, Conversion of CO2 and H2 into propane over InZrOx and SSZ-13 composite catalyst, J. Energy Chem. 54 (2021) 111–117.

[48] J. Chen, X. Wang, D. Wu, J. Zhang, Q. Ma, X. Gao, X. Lai, H. Xia, S. Fan, T.-S. Zhao, Hydrogenation of CO2 to light olefins on CuZnZr@(Zn-) SAPO-34 catalysts: Strategy for product distribution, Fuel 239 (2019) 44–52.

[49] I.M. Dahl, H. Mostad, D. Akporiaye, R. Wendelbo, Structural and chemical influences on the MTO reaction: a comparison of chabazite and SAPO-34 as MTO catalysts, Micropor. Mesopor. Mater. 29 (1999) 185–190.

[50] S. Nawaz, S. Kolboe, S. Kvisle, K. Lillerud, M. Stocker, H. Øren, Selectivity and deactivation profiles of zeolite type materials in the MTO process, Stud. Surf. Sci. Catal. Elsevier (1991) 421–427.

[51] E.C. Ra, K.H. Kim, J.H. Lee, S. Jang, H.E. Kim, J.H. Lee, E.H. Kim, H. Kim, J. H. Kwak, J.S. Lee, Selective light hydrocarbon production from CO2 hydrogenation over Na/ZnFe2O4 and CHA-Zeolite hybrid catalysts, ACS Catal. 14 (2024) 3492–3503.

[52] S. Brunauer, P.H. Emmett, E. Teller, Adsorption of gases in multimolecular layers, J. Am. Chem. Soc. 60 (1938) 309–319.

[53] I. Anton Paar QuantaTec, Instruction Manual and Safety Information, autosorb iQ Gas Sorption SystemGraz, Austria, 2022.

[54] S. Kozuch, J.M. Martin, "Turning over" definitions in catalytic cycles, ACS Publications (2012) 2787–2794.

[55] M.A. Deimund, L. Harrison, J.D. Lunn, Y. Liu, A. Malek, R. Shayib, M.E. Davis, Effect of heteroatom concentration in SSZ-13 on the methanol-to-olefins reaction, ACS Catal. 6 (2016) 542–550.

[56] Y. Jiang, J. Huang, V.R. Marthala, Y.S. Ooi, J. Weitkamp, M. Hunger, In situ MAS NMR–UV/Vis investigation of H-SAPO-34 catalysts partially coked in the methanol-to-olefin conversion under continuous-flow conditions and of their regeneration, Micropor. Mesopor. Mater. 105 (2007) 132–139.

[57] F. Mahnaz, J.R. Mangalindan, B.C. Dharmalingam, J. Vito, Y.-T. Lin, M. Akbulut, J. J. Varghese, M. Shetty, Intermediate transfer rates and solid-state ion exchange are key factors determining the bifunctionality of In2O3/HZSM-5 tandem CO2 hydrogenation catalyst, ACS Sust. Chem. Eng. (2024).

[58] I. Nezam, W. Zhou, G.S. Gusmão, M.J. Realff, Y. Wang, A.J. Medford, C.W. Jones, Direct aromatization of CO2 via combined CO2 hydrogenation and zeolite-based acid catalysis, J. CO2 Util. 45 (2021) 101405.

[59] J. Li, Z. Wei, Y. Chen, B. Jing, Y. He, M. Dong, H. Jiao, X. Li, Z. Qin, J. Wang, A route to form initial hydrocarbon pool species in methanol conversion to olefins over zeolites, J. Catal. 317 (2014) 277–283.

[60] Y. Liu, F.M. Kirchberger, S. Müller, M. Eder, M. Tonigold, M. Sanchez-Sanchez, J. A. Lercher, Critical role of formaldehyde during methanol conversion to hydrocarbons, Nat. Commun. 10 (2019) 1462.

[61] P. Huber, P.N. Plessow, The role of decarboxylation reactions during the initiation of the methanol-to-olefins process, J. Catal. 428 (2023) 115134.

[62] Z. Wei, Y.-Y. Chen, J. Li, P. Wang, B. Jing, Y. He, M. Dong, H. Jiao, Z. Qin, J. Wang, Methane formation mechanism in the initial methanol-to-olefins process catalyzed by SAPO-34, Catalysis, Sci. Technol. 6 (2016) 5526–5533.

[63] O. Dewaele, V.L. Geers, G.F. Froment, G.B. Marin, The conversion of methanol to olefins: a transient kinetic study, Chem. Eng. Sci. 54 (1999) 4385–4395.

[64] L. Kubelková, J. Nováková, P. Jírů, Reaction of small amounts of methanol on Hzsm-5, Hy and modified Y zeolites, Studies in Surface Science and Catalysis, Elsevier1984, pp. 217-224.

[65] E.J. Munson, N.D. Lazo, M.E. Moellenhoff, J.F. Haw, Carbon monoxide is neither an intermediate nor a catalyst in MTG chemistry on zeolite HZSM-5, J. Am. Chem. Soc. 113 (1991) 2783–2784.

[66] G.J. Hutchings, R. Hunter, P. Johnston, L.J. Vanrensburg, Methanol conversion to hydrocarbons over Zeolite H-ZSM-5: investigation of the role of CO and ketene in the formation of the Initial C–C bond, J. Catal. 142 (1993) 602–616.

[67] Q. Ma, T. Fu, L. Yin, Z. Li, Constructing macroscopic core@ shell catalyst to boost tandem catalysis of methanol to aromatic, Chem. Eng. J. 462 (2023) 142252.

[68] T. Xie, J. Ding, X. Shang, X. Zhang, Q. Zhong, Effective synergies in indium oxide loaded with zirconia mixed with silicoaluminophosphate molecular sieve number 34 catalysts for carbon dioxide hydrogenation to lower olefins, J. Colloid Interface Sci. 635 (2023) 148–158.

[69] Y. Yuan, R.F. Lobo, Propane dehydrogenation over extra-framework In (i) in chabazite zeolites, Chem. Sci. 13 (2022) 2954–2964.

[70] Z. Liu, J. Cheng, O. Höfft, F. Endres, Electrodeposition of indium from an ionic liquid investigated by in situ electrochemical XPS, Metals 12 (2021) 59.

[71] E. Miró, L. Gutiérrez, J.R. López, F. Requejo, Perturbed angular correlation characterization of indium species on In/H-ZSM5 catalysts, J. Catal. 188 (1999) 375–384.

[72] A.A. Gabrienko, S.S. Arzumanov, I.B. Moroz, I.P. Prosvirin, A.V. Toktarev, W. Wang, A.G. Stepanov, Methane activation on in-modified ZSM-5: the state of indium in the zeolite and pathways of methane transformation to surface species, J. Phys. Chem. C 118 (2014) 8034–8043.

[73] M.H. Kim, I.H. Cho, J.H. Park, S.O. Choi, I.-S. Lee, Adsorption of CO 2 and CO on H-zeolites with different framework topologies and chemical compositions and a correlation to probing protonic sites using NH 3 adsorption, J. Porous Mater. 23 (2016) 291–299.

[74] H. Zhao, M. Lin, Y. Wang, J. Zheng, Effect of hydrothermal aging temperature on a Cu-SSZ-13/H-SAPO-34 composite for the selective catalytic reduction of NO x by NH 3, RSC Adv. 11 (2021) 33334–33343.

[75] J.M. Zamaro, E.E. Miró, A.V. Boix, A. Martínez-Hernández, G.A. Fuentes, In–zeolites prepared by oxidative solid state ion exchange (OSSIE): Surface species and structural characterization, Micropor. Mesopor. Mater. 129 (2010) 74–81.

[76] D.V. Shinde, V.V. Jadhav, D.Y. Lee, N.K. Shrestha, J.K. Lee, H.Y. Lee, R.S. Mane, S.-H. Han, A coordination chemistry approach for shape controlled synthesis of indium oxide nanostructures and their photoelectrochemical properties, J. Mater. Chem. A 2 (2014) 5490–5498.

[77] Z. Maeno, S. Yasumura, X. Wu, M. Huang, C. Liu, T. Toyao, K.-I. Shimizu, Isolated indium hydrides in CHA zeolites: speciation and catalysis for nonoxidative dehydrogenation of ethane, J. Am. Chem. Soc. 142 (2020) 4820–4832.

[78] A. Kyndiah, A. Ablat, S. Guyot-Reeb, T. Schultz, F. Zu, N. Koch, P. Amsalem, S. Chiodini, T. Yilmaz Alic, Y. Topal, A multifunctional interlayer for solution processed high performance indium oxide transistors, Sci. Rep. 8 (2018) 10946.

[79] H. Beyer, R. Mihályi, C. Minchev, Y. Neinska, V. Kanazirev, Study of the reductive solid-state ion exchange of indium into NH4NaY zeolite, Micropor. Mater. 7 (1996) 333–341.

[80] R. Mihalyi, H. Beyer, V. Mavrodinova, C. Minchev, Y. Neinska, Study of the reductive solid-state ion exchange of indium into an NH4-beta zeolite, Micropor. Mesopor. Mater. 24 (1998) 143–151.

[81] R. Mihályi, Z. Schay, Á. Szegedi, Preparation of In, H-ZSM-5 for DeNOx reactions by solid-state ion exchange, Catal. Today 143 (2009) 253–260.